UNIVERSIDAD DE CONCEPCIÓN

Centro de Investigación en Ingeniería Matemática (CI^{2}MA)

Modeling and numerical simulation of the colonization of plant growth-promoting bacteria in the rice rhizosphere

Idulfo Arrocha, Raimund Bürger,
María Gómez, Yolanda Vásquez

PREPRINT 2026-21

SERIE DE PRE-PUBLICACIONES

MODELING AND NUMERICAL SIMULATION OF THE COLONIZATION OF PLANT GROWTH-PROMOTING BACTERIA IN THE RICE RHIZOSPHERE

IDULFO ARROCHA[A,B], RAIMUND BÜRGER[C], MARÍA GÓMEZ[A,*], AND YOLANDA VÁSQUEZ[A,B,D]

Abstract. In Panama, rice (*Oryza sativa* L.) production entails high economic and environmental costs due to a heavy dependence on chemical fertilizers. As a sustainable alternative, the use of plant growth-promoting rhizobacteria (PGPR) is being evaluated, but its successful deployment requires a quantitative understanding of how inoculated bacteria spread and colonize the highly competitive rhizosphere. Since this process is complex and expensive to study experimentally, we formulate and solve numerically a mathematical model, based on a system of coupled partial differential equations, for the spatiotemporal dynamics of PGPR in response to root exudation. The spatially two-dimensional domain arises from an axisymmetric cylindrical coordinate system and incorporates a moving boundary representing the growing rice root. The model couples a reaction-diffusion equation for the substrate (root exudates) with a reaction-diffusion-advection equation for the bacterial biomass, combining Monod growth kinetics with directed motility through chemotaxis of Keller–Segel type. Approximate solutions are computed by a finite volume spatial discretization and an implicit-explicit time-integration algorithm designed to be positivity preserving. The scheme is validated against the classical one-dimensional steady-state scenario of Newman and Watson (1977). Two-dimensional simulations based on literature parameters reveal that chemotaxis and the substrate diffusion coefficient are the dominant factors governing colonization efficiency, and exhibit a temporal lag in biomass growth as well as the inability of the population to instantly colonize newly formed root tissue at the growing tip. The model provides a predictive tool for evaluating inoculation strategies and optimizing PGPR use in sustainable agriculture.

1. Introduction

1.1. **Scope.** Rice (*Oryza sativa* L.) is one of the most widely consumed staple crops in the world and a pillar of food security in Panama, where the country sows over 100,000 hectares annually [1]. Production costs per hectare have oscillated between US$2,300 and 2,700 in recent years [2], driven in large part by a heavy dependence on chemical fertilizers needed to compensate for the naturally low fertility of most Panamanian soils. Beyond economics, this dependence carries significant environmental consequences, motivating the search for sustainable agronomic alternatives. One such alternative is the use of plant growth-promoting rhizobacteria (PGPR). These are naturally

Date: June 26, 2026.

Key words and phrases. plant growth-promoting bacteria; rhizosphere; chemotaxis; reaction-diffusion-advection; finite volume method; moving boundary; Keller–Segel model.

*Corresponding author.

[A]Facultad de Ciencias y Tecnología, Universidad Tecnológica de Panamá, Ricardo J. Alfaro Avenue, Dr. Victor Levi Sasso University Campus, Panama 0819-07289, Panama. E-Mail: idulfo.arrocha@utp.ac.pa, maria.gomez10@utp.ac.pa, yolanda.vasquez@utp.ac.pa.

[B]Centro de Estudios Multidisciplinarios en Ciencias, Tecnología e Ingeniería, Ricardo J. Alfaro Avenue, Dr. Victor Levi Sasso University Campus, Panama 0819-07289, Panama.

[C]CI^{2}MA and Departamento de Ingeniería Matemática, Facultad de Ciencias Físicas y Matemáticas, Universidad de Concepción, Casilla 160-C, Concepción, Chile. E-Mail: rburger@ing-mat.udec.cl.

[D]SNI-SENACYT Sistema Nacional de Investigación–Secretaría Nacional de Ciencia, Tecnología e Innovación, Ciudad del Saber, Building 205, Clayton, Panama 0816-02852, Panama.

occurring soil microorganisms that colonize the narrow soil region surrounding the root system, the rhizosphere [3], and contribute to plant development through a variety of mechanisms. According to Ahemad and Kibret [4], effective PGPR strains must be capable of colonizing the root surface, surviving and reproducing competitively in the rhizosphere for a sufficient period to exert their beneficial effects, and actively promoting plant growth. Their beneficial action operates through several channels: acting as biofertilizers by facilitating the availability of essential nutrients such as nitrogen and phosphorus, functioning as biocontrol agents by inhibiting soil-borne pathogens, and increasing the absorption of micronutrients such as iron and zinc [5]. Recent studies further highlight their potential for the bioremediation of contaminated soils [6].

The rhizosphere is enriched by a continuous flux of carbon-containing compounds and signaling molecules secreted by the root, collectively known as root exudates [7, 8]. These exudates serve as chemical attractants that drive microbial migration toward the root surface, creating a reciprocal relationship between root activity and microbial community dynamics [9]. In the context of rice, field studies have confirmed that PGPR strains promote increases in root length [10], improve plant resilience under water stress [11], and enhance grain yield [12]. In particular, a study conducted at the Institute of Agricultural Innovation of Panama (IDIAP) [12] isolated two strains, *Lysinibacillus fusiformis* and *Bacillus cereus*, from local soils and demonstrated, via inoculation of rice seeds, that these bacteria promote plant growth and increase spike grain weight. However, despite these promising results, optimizing PGPR bioinoculants remains a significant scientific challenge. The rhizosphere is a highly dynamic and competitive ecological niche: inoculated bacteria must establish and proliferate in competition with the native microbial community, and this process is governed by a delicate interplay between microbial growth kinetics, substrate availability, and the capacity for directed movement. Directly studying these interactions under controlled conditions requires specialized equipment and considerable investment currently unavailable in Panama and elsewhere, which motivates mathematical modeling as a cost-effective alternative. By expressing the biological and physical processes of the rhizosphere as a system of partial differential equations (PDEs), one can simulate and predict bacterial behavior, identify critical parameters, and evaluate inoculation strategies *in silico* before committing to costly experiments.

It is the purpose of this contribution to develop and numerically simulate a two-dimensional mathematical model of PGPR colonization in the rice rhizosphere. The model tracks the axisymmetric spatio-temporal evolution of two coupled variables: the substrate concentration $S = S(r, z, t)$ representing root exudates, and the bacterial biomass $B = B(r, z, t)$, where r is the radial coordinate (with respect to the centerline of the root as axis of symmetry), z is depth, and t is time. The evolution of S and B is governed by the PDE system

$$\frac{\partial S}{\partial t} = D\Delta S - \left(\frac{\mu(S)}{Y} + m(S)\right) B, \tag{1.1a}$$

$$\frac{\partial B}{\partial t} = \sigma\Delta B - \nabla\cdot(\chi B\nabla S) + \big(\mu(S) - \delta\big)B, \tag{1.1b}$$

where D and σ are the diffusion and bacterial motility coefficients, χ is the chemotactic sensitivity, δ is the bacterial decay rate, Y is the yield coefficient, $\mu(S)$ is the growth function which is usually chosen according to the Monod expression

$$\mu(S) \coloneqq \mu_{\max}\frac{S}{S + \rho K_{\mathrm{s}}}, \tag{1.2}$$

and $m(S)$ is the maintenance rate function given by

$$m(S) \coloneqq \min\{\kappa S, m_0\}, \tag{1.3}$$

where κ is a positive constant and m_0 is the constant maintenance rate wherever there is sufficient supply of substrate. Notice that $m(S) = m_0$ whever $S \geq m_0/\kappa$. The particular form (1.3) has been chosen to ensure that $S \geq 0$ and $B \geq 0$, under suitable initial and boundary conditions. The assumption (1.3) is physically reasonable since the consumption of substrate due to cell viability cannot exceed the available substrate.

The domain is defined in cylindrical coordinates (r, z) with a moving boundary at $z = L_R(t)$ tracking the growing root tip. In these coordinates the Laplacian becomes

$$\Delta S = \frac{1}{r}\frac{\partial}{\partial r}\left(r\frac{\partial S}{\partial r}\right) + \frac{\partial^2 S}{\partial z^2} \tag{1.4}$$

(analogously for ΔB) while

$$\nabla \cdot (\chi B \nabla S) = \frac{1}{r}\frac{\partial}{\partial r}\left(r\chi B\frac{\partial S}{\partial r}\right) + \frac{\partial}{\partial z}\left(\chi B\frac{\partial S}{\partial z}\right). \tag{1.5}$$

A Neumann exudation flux is imposed at the lateral root surface $r = a$, and homogeneous Neumann (no-flux) conditions hold on all remaining boundaries.

1.2. **Related work.** To put this contribution into the proper perspective we first recall that the rhizosphere is characterized by intense microbial activity driven by the continuous release of root exudates: complex mixtures of sugars, amino acids, and secondary metabolites that provide a carbon substrate for microbial growth [4, 7]. The exudation creates a chemical gradient that is the primary driver of PGPR migration toward the root. A comprehensive review of rhizosphere models up to 2021 by Kuppe et al. [13] classifies existing mathematical models along two axes of increasing complexity: the treatment of solute (substrate) transport and the treatment of microbial dynamics. Most existing models rely on ordinary differential equations (ODEs) and neglect spatial transport entirely [14, 15]; these describe temporal population dynamics but cannot capture the spatial colonization patterns that are central to inoculant optimization.

The first PDE-based model for substrate dynamics in the rhizosphere was introduced by Newman and Watson [16] who adopted a one-dimensional cylindrical geometry with the root modeled as a straight cylinder of radius a. Their model describes the radial diffusion of substrate from the root surface and its consumption by a static microbial population, so that the model is specified by only one PDE for S, namely

$$\frac{\partial S}{\partial t} = \frac{D}{r}\frac{\partial}{\partial r}\left(r\frac{\partial S}{\partial r}\right) - \frac{\mu_{\max}}{Y}\frac{MS}{S + K_s\theta} + CM_0, \tag{1.6}$$

where M is the (fixed) microbial concentration, θ the soil water content, and C the maintenance coefficient. The consumption rate (i.e., the term with minus sign in the right-hand side of (1.6)) follows Michaelis-Menten kinetics [17], whereby the uptake rate saturates at high substrate concentrations. Although (1.6) laid the conceptual foundation for rhizosphere modeling, it treats bacteria as immobile and does not account for their directed movement. Similarly, de Parseval et al. [18] model the physical substrate environment using PDEs but exclude bacterial dynamics entirely.

The broader theoretical framework for spatially explicit bacterial dynamics originates in the reaction-diffusion paradigm established by Turing [19], who showed that interacting diffusing substances can generate complex patterns from uniform states. In microbial contexts, Kawasaki et al. [20] and Mimura et al. [21] demonstrated that *Bacillus subtilis* exhibits five distinct colony morphologies depending on medium hardness and nutrient levels; in soft media with abundant substrate, colonies expand as uniform discs. To capture sharper colonization fronts, Lacasta et al. [22] proposed nonlinear diffusion terms reflecting density-dependent motility. Beyond passive diffusion,

bacteria possess a directed sensory response to chemical gradients known as chemotaxis [23], which can be modeled as an advective transport term. The continuum formulation was introduced by Keller and Segel [24], whose well-known model for the bacterial density B reads

$$\frac{\partial B}{\partial t} = \nabla \cdot (\sigma \nabla B) - \nabla \cdot (\chi\, B\, \nabla S), \tag{1.7}$$

where the first term describes random motility and the second models advection up the substrate gradient. Reviews of Keller–Segel chemotaxis models are provided by Arumugam and Tyagi [25] and Hillen and Painter [26], who explain how the chemotaxis term can be derived from individual random-walk processes with a biased response to chemical signals. Leyva et al. [27] showed via reaction-diffusion-chemotaxis models that this directed response not only orients colonization but significantly accelerates the advance of the bacterial front, ensuring the population can track nutrient gradients before they are depleted. The global solvability of chemotaxis systems where the chemical is consumed by the cells was analyzed by Lankeit and Lankeit [28].

Combining components of both (1.6) and (1.7), Dupuy and Silk [29] developed the most complete one-dimensional rhizosphere model to date (cf., e.g., [13]). This model couples substrate diffusion with bacterial chemotaxis and models root exudation from the tip. The present work builds directly on this coupled framework and extends it in three directions: (i) the spatial domain is extended to two dimensions in an axisymmetric cylindrical geometry; (ii) a time-varying root length is incorporated via a moving boundary; and (iii) the bacterial equation includes Monod growth and decay kinetics, making the two equations fully coupled.

With respect to numerical methods we mention that the finite volume method (FVM) [30, 31] is a natural choice for the spatial discretization, as it enforces local mass conservation on each control volume directly from the integral form of the corresponding conservation law [32]. Centered differences are used for the diffusive fluxes, while the chemotactic (advective) term is handled by a first-order upwind scheme [33], which preserves positivity of the bacterial biomass and avoids spurious oscillations near sharp concentration gradients [34]. The temporal integration follows is done by a splitting method that treats the stiff diffusion operators, the convection term in the PDE for B, and one of the nonlinear reaction terms implicitly [35, 36]. This methodology leads to a sparse linear system solved at each time step via $\boldsymbol{LU}$ factorization for the diffusion and chemotactic movemet step. The implicit treatment of one of the reaction terms does not require to solve equations at all (in case of the Monod kinetics); rather, the scheme can be written in an explicit form since only a quadratic equation needs to be solved. The positivity of the numerical solution is established through an M-matrix analysis of the linear systems, in the spirit of the invariant region preserving schemes developed by the authors for a related convection diffusion system [37], and using arguments similar to those of Bürger et al. [38] and Acosta et al. [39]. Finally, the moving root boundary is tracked on a fixed mesh using the cut-cell technique of Bürger et al. [40], which modifies cell areas and volumes in the layer intersected by the root tip without the need for remeshing.

1.3. **Outline of the paper.** The remainder of this paper is organized as follows. Section 2 presents the mathematical model in detail: the physical problem, the axisymmetric cylindrical domain, the moving root boundary, the governing PDE system (1.1) with its boundary and initial conditions, and the model parameters. Section 3 describes the numerical scheme, including the FVM spatial discretization for both the substrate and bacterial equations (with upwind chemotaxis treatment and cut-cell moving boundary correction) and the implicit-explicit splitting time integration algorithm. In particular we explicitly prove that the method is positivity preserving, which means that the simulated substrate and bacteria densities always remain non-negative. Section 4 presents

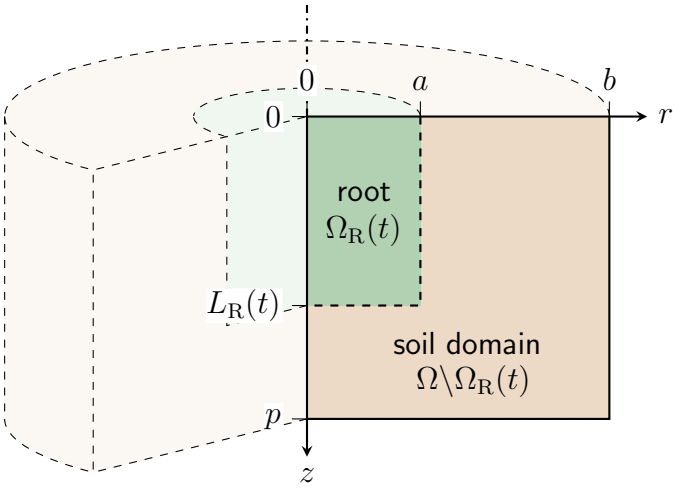

FIGURE 1. Physical domain Ω in cylindrical coordinates (r, z). The horizontal r-axis spans the rhizosphere radius ($0 \le r \le b$) and the vertical z-axis the soil depth ($0 \le z \le p$). The green-marked upper-left region represents the root subdomain $\Omega_{\mathrm{R}}(t)$, defined by the root radius a and the time-varying depth $L_{\mathrm{R}}(t)$.

the numerical results, starting with a validation against the classical one-dimensional steady-state scenario of Newman and Watson [16], followed by two-dimensional simulations that explore the effect of chemotaxis, substrate diffusivity, bacterial motility, and initial inoculation density on colonization patterns over a 30-day period. Section 5 summarizes the main findings and proposes directions for future work.

2. Mathematical model

2.1. **Physical formulation and domain.** The model describes the dynamics of substrate $S(r, z, t)$ (root exudates) and bacterial biomass $B(r, z, t)$ in the soil surrounding a growing rice root. The root is modeled as a smooth vertical cylinder of radius a that elongates downward over time, a simplification that allows the complex three-dimensional geometry to be reduced to a tractable two-dimensional problem (see Figure 1). Because the root is cylindrical and the exudation flux is assumed to be uniform along the root wall, the system is axisymmetric with respect to the root axis; the solution is therefore independent of the azimuthal angle and can be fully described in the meridional plane.

The soil region constitutes the rhizosphere, and is represented by the two-dimensional domain

$$\Omega := \big\{(r, z) \in \mathbb{R}^2 \,:\, 0 \le r \le b, \quad 0 \le z \le p\big\}, \tag{2.1}$$

where r denotes the radial distance from the root axis, z the soil depth (positive downward), b the rhizosphere radius, and p the total soil depth considered. The root occupies the time-dependent subdomain

$$\Omega_{\mathrm{R}}(t) := \big\{(r, z) \in \mathbb{R}^2 \,:\, 0 \le r \le a, \quad 0 \le z \le L_{\mathrm{R}}(t)\big\},$$

where $L_{\mathrm{R}}(t)$ is the root length at time t. The soil domain available for diffusion and bacterial colonization is then $\Omega\backslash\Omega_{\mathrm{R}}(t)$; see Figure 1.

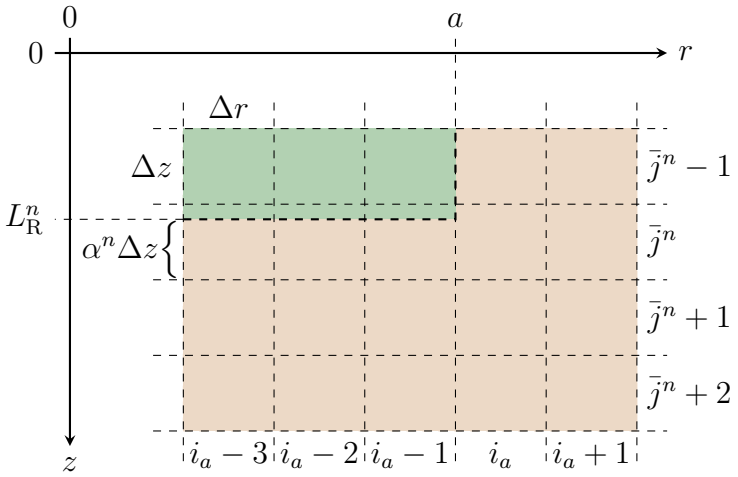

FIGURE 2. Cut-cell discretization of the root–soil interface at time t_n. The index $\bar{j}^n$ identifies the cell containing the root tip, and the fraction α^n quantifies the soil-occupied portion of that cell.

2.2. **Moving boundary due to root growth.** The elongation of the root is modeled by the saturation law

$$L_{\mathrm{R}}(t) = l(1 - \mathrm{e}^{-\beta t}), \quad l, \beta > 0, \tag{2.2}$$

where l [cm] is the asymptotic root length and β [h^{-1}] is the initial elongation rate ($\dot{L}_{\mathrm{R}}(0) = l\beta$) [14]. This expression reproduces rapid growth after germination followed by exponential deceleration toward the asymptote l.

The moving boundary is implemented on a fixed computational grid using the cut-cell approach by Bürger et al. [40]. At each time step t_n, the index of the grid cell that contains the root tip is $\bar{j}^n := \lceil L_{\mathrm{R}}^n / \Delta z \rceil$, and the fraction of that cell occupied by soil (not by root) is

$$\alpha^n := \left(z_{\bar{j}^n + 1/2} - L_{\mathrm{R}}^n \right) / \Delta z.$$

The fraction α^n is used in the discretization (Section 3) to scale the effective volumes and face areas of the cut cell, allowing the root tip to advance without remeshing; see Figure 2.

2.3. **Root exudation.** Root exudation is described by a spatio-temporally varying flux that reflects the age-dependent metabolic activity of the root tissue. Following Schwalm et al. [41], we utilize the exudation rate function

$$Q(z,t) = Q_{\mathrm{m}} \mathrm{e}^{-d\tau(z,t)} H\big(\tau(z,t)\big), \tag{2.3}$$

where Q_{m} [$\mu\mathrm{g\,cm^{-2}\,h^{-1}}$] is the maximum exudation rate, d [h^{-1}] is the decay rate of exudation with root age, and $\tau(z,t) := t - T(z)$ is the age of the root tissue at depth z and time t. Here $T(z) = -(1/\beta)\ln(1 - z/l)$ is the time at which the root tip first reached depth z (obtained by using (2.2) to solve $L_{\mathrm{R}}(t) = z$ for t), and H is the Heaviside step function used here to ensure that no exudation occurs at depths not yet reached by the root ($\tau < 0$). Thus, the flux decreases exponentially with tissue age, reflecting the known reduction in exudate secretion in older, more mature root zones.

2.4. **Model assumptions and governing equations.** The following simplifying assumptions are adopted to make the model analytically and computationally tractable:

(A1) *Root geometry.* The root is a smooth straight cylinder. Lateral branches, root hairs, and surface roughness are neglected; exudation is spatially uniform across the cylindrical wall.
(A2) *Soil properties.* The soil is a homogeneous, isotropic porous medium with constant porosity; spatial variations in bulk density, aggregate structure, and moisture content are neglected.
(A3) *Axisymmetry.* Both the exudation flux and the bacterial distribution are symmetric with respect to the root axis, reducing the problem to the two-dimensional domain (2.1).
(A4) *Transport mechanisms.* Substrate and bacteria move through the soil by diffusion; bacterial cells additionally exhibit directed motion (chemotaxis) up the substrate gradient. Advective water flow due to root uptake is neglected; soil moisture is constant and optimal for biological activity.
(A5) *Single limiting substrate.* Following Newman and Watson [16], root exudate carbon is the sole nutrient limiting bacterial growth; other nutrients and oxygen are assumed non-limiting.
(A6) *Linear chemotaxis.* The chemotactic velocity is proportional to the substrate gradient [24], without receptor saturation effects.
(A7) *Single bacterial population.* Only the interactions between the root and one bacterial species are modeled; competition with native microorganisms, predation, and biofilm formation are excluded.

Under assumptions (A1)–(A7), the spatiotemporal dynamics of substrate $S = S(r, z, t)$ and bacterial biomass $B = B(r, z, t)$ are governed by the coupled PDE system (1.1) along with the Monod growth function (1.2). The first term on the right-hand side of (1.1a) describes Fickian diffusion of the substrate; the remaining terms represent consumption by the bacterial population through growth and cellular maintenance. In (1.1b), the first term on the right-hand side accounts for random bacterial motility, the second for directed migration up the substrate gradient (chemotaxis), and the last for population growth and decay. Taking into account (1.4) and (1.5) we may rewrite (1.1) as

$$\frac{\partial S}{\partial t} = D\left(\frac{1}{r}\frac{\partial}{\partial r}\left(r\frac{\partial S}{\partial r}\right) + \frac{\partial^2 S}{\partial z^2}\right) - \left(\frac{\mu(S)}{Y} + m(S)\right)B, \tag{2.4a}$$

$$\frac{\partial B}{\partial t} = \sigma\left(\frac{1}{r}\frac{\partial}{\partial r}\left(r\frac{\partial B}{\partial r}\right) + \frac{\partial^2 B}{\partial z^2}\right) - \frac{1}{r}\frac{\partial}{\partial r}\left(r\chi B\frac{\partial S}{\partial r}\right) - \frac{\partial}{\partial z}\left(\chi B\frac{\partial S}{\partial z}\right) + \big(\mu(S) - \delta\big)B. \tag{2.4b}$$

System (2.4) represents a bidirectional coupling: bacteria migrate chemotactically toward zones of higher substrate concentration, while the substrate is depleted by bacterial consumption. The steady-state distribution of biomass around the root depends on the balance between the exudation rate $Q(z, t)$, the transport coefficients D, σ, χ, and the biological kinetic parameters.

2.5. **Parameters.** Table 1 lists all variables and parameters of system (2.4) together with their units. The yield coefficient Y and maintenance rate m_0 govern the metabolic efficiency of the bacteria: Y converts consumed substrate into new biomass, while m_0 represents the energy cost for cell viability independent of growth.

The bioavailability factor ρ accounts for the fact that in compacted soils a fraction of the substrate is physically inaccessible to the bacteria [16]. The ratio χ/σ between the chemotactic sensitivity and the random motility quantifies the degree of directedness in bacterial migration: large values indicate that bacteria move preferentially up chemical gradients rather than diffusing randomly [29]. The exudation decay parameters Q_{m} and d control the spatiotemporal heterogeneity of the

TABLE 1. Variables and parameters of the soil–root–bacteria system.

Symbol	Description	Units
State variables		
$S(r,z,t)$	Substrate (exudate) concentration	$\mu g\,cm^{-3}$
$B(r,z,t)$	Bacterial biomass concentration	$\mu g\,cm^{-3}$
Transport and chemotaxis		
D	Substrate diffusion coefficient	$cm^2\,h^{-1}$
σ	Bacterial motility coefficient	$cm^2\,h^{-1}$
χ	Chemotactic sensitivity	$cm^5\,\mu g^{-1}\,h^{-1}$
Monod growth kinetics		
κ	Parameter in maintenance rate function	
$\mu_{\max}$	Maximum specific growth rate	h^{-1}
K_s	Half-saturation constant	$\mu g\,cm^{-3}$
ρ	Substrate bioavailability factor	dimensionless
Y	Yield coefficient	dimensionless
m_0	Cell maintenance rate constant	h^{-1}
δ	Bacterial decay rate	h^{-1}
Root dynamics and exudation		
l	Asymptotic root length	cm
β	Root elongation rate	h^{-1}
Q_{m}	Maximum exudation rate	$\mu g\,cm^{-2}\,h^{-1}$
d	Exudation decay rate	h^{-1}
a	Root radius	cm
b	Rhizosphere radius	cm

substrate source, distinguishing young, metabolically active root tissue near the tip from older, mature zones [41].

2.6. **Initial and boundary conditions.** The substrate equation (2.4a) requires a Neumann boundary condition at the lateral root surface $r = a$ to model exudation. We impose

$$-D\,\frac{\partial S}{\partial r}\bigg|_{r=a} = Q(z,t), \tag{2.5}$$

where $Q(z,t)$ is defined in (2.3). Homogeneous Neumann (no-flux) conditions are imposed on all other boundaries:

$$\frac{\partial S}{\partial r}\bigg|_{r=b} = \frac{\partial S}{\partial r}\bigg|_{r=0} = \frac{\partial S}{\partial z}\bigg|_{z=0} = \frac{\partial S}{\partial z}\bigg|_{z=p} = 0. \tag{2.6}$$

For the bacterial equation (2.4b), no-flux conditions hold on all boundaries:

$$\frac{\partial B}{\partial r}\bigg|_{r=b} = \frac{\partial B}{\partial r}\bigg|_{r=0} = \frac{\partial B}{\partial z}\bigg|_{z=0} = \frac{\partial B}{\partial z}\bigg|_{z=p} = 0. \tag{2.7}$$

Initial conditions at $t = 0$ are uniform:

$$S(r,z,0) = S_0, \qquad B(r,z,0) = B_0,$$

where S_0 and B_0 are the initial substrate and biomass concentrations, respectively.

2.7. **Mathematical character of the PDE system.** System (2.4) is a nonlinear coupled system of reaction-diffusion-advection type of a particular parabolic character that directly determines the choice of the numerical method. The diffusion terms $D\Delta S$ and $\sigma\Delta B$ confer a parabolic character, ensuring smooth propagation of information and a tendency toward steady state when exudation ceases. These stiff terms are treated implicitly in the time integrator. The chemotaxis term $-\nabla\cdot(\chi B\,\nabla S)$ arising in (1.1b) acts as a directed advection term for B if we suppose that S is given. For large χ, this term dominates and creates sharp concentration fronts that, if treated with centered differences, produce nonphysical oscillations; an upwind discretization is therefore required. Finally, the Monod nonlinear reaction terms introduce a strong nonlinear coupling between S and B. As stiff reaction terms, and to ensure positivity of the numerical solution values, they require implicit or semi-implicit treatment to avoid prohibitively small time steps. This treatment is incorporated in the splitting scheme introduced in the next section.

3. Numerical scheme

3.1. **Spatial mesh and control volumes.** Let N_r and N_z be the number of cells in the radial and axial directions, respectively, with uniform mesh widths $\Delta r = b/N_r$ and $\Delta z = p/N_z$. Cell-center coordinates are

$$r_i \coloneqq (i-1/2)\Delta r, \quad i=1,\dots,N_r; \quad z_j \coloneqq (j-1/2)\Delta z, \quad j=1,\dots,N_z,$$

and cell-face coordinates are $r_{i\pm1/2} \coloneqq r_i \pm \Delta r/2$ and $z_{j\pm1/2} \coloneqq z_j \pm \Delta z/2$. Due to axisymmetry (assumption A3), each cell $V_{i,j}$ represents a three-dimensional annular sector of unit radian with volume

$$\Delta V_{i,j} = \int_{r_{i-1/2}}^{r_{i+1/2}} \int_{z_{j-1/2}}^{z_{j+1/2}} r\,\mathrm{d}r\,\mathrm{d}z = r_i \Delta r \Delta z,$$

and face areas

$$A_{r,i\pm1/2} \coloneqq r_{i\pm1/2}\Delta z \quad \text{(radial faces) and} \quad A_{z,i} \coloneqq r_i \Delta r \quad \text{(axial faces).} \tag{3.1}$$

Furthermore, we define the reaction terms

$$R_S(S,B) \coloneqq -\left(\frac{\mu(S)}{Y} + m(S)\right) B, \quad R_B(S,B) \coloneqq \big(\mu(S)-\delta\big)B.$$

3.2. **Semi-discrete scheme for the substrate equation.** The substrate flux vector is $\boldsymbol{F} = D\,\nabla S$. Integrating (2.4a) over $V_{i,j}$, applying the divergence theorem, and approximating interface fluxes by centered differences, we obtain that the cell volumes cancel and we obtain the semi-discrete equation

$$\begin{aligned}\frac{\mathrm{d}S_{i,j}}{\mathrm{d}t} = \frac{D}{\Delta V_{i,j}}\Bigg(&\frac{S_{i-1,j}-S_{i,j}}{\Delta r}A_{r,i-1/2} - \frac{S_{i,j}-S_{i+1,j}}{\Delta r}A_{r,i+1/2} \\ &+ \frac{S_{i,j-1}-S_{i,j}}{\Delta z}A_{z,i} - \frac{S_{i,j}-S_{i,j+1}}{\Delta z}A_{z,i}\Bigg) + R_S(S_{i,j},B_{i,j}).\end{aligned} \tag{3.2}$$

The exudation boundary condition (2.5) is imposed by replacing the centered-difference flux at the face $r_{i_a-1/2} = a$ (where i_a is the index of the innermost soil cell) with the prescribed value $Q(z_j,t)$; this introduces a source term $\boldsymbol{E}$ that is nonzero only for cells (i_a,j) adjacent to the root. Suppose

$(e_{i,j})$ are the entries of $\boldsymbol{E}$. Then we get for $i = i_a$, instead of (3.2),

$$\begin{aligned}\frac{\mathrm{d}S_{i_a,j}}{\mathrm{d}t} = \frac{D}{\Delta V_{i_a,j}}\Bigg(&-\frac{S_{i_a,j}-S_{i_a+1,j}}{\Delta r}A_{r,i_a+1/2} + \frac{S_{i_a,j-1}-S_{i_a,j}}{\Delta z}A_{z,i} - \frac{S_{i_a,j}-S_{i_a,j+1}}{\Delta z}A_{z,i}\Bigg)\\ &+ R_S(S_{i_a,j},B_{i_a,j}) + e_{i_a,j},\end{aligned} \tag{3.3}$$

where we define

$$e_{i,j} \coloneqq \begin{cases} Q(z_j,t)A_{r,i_a-1/2}/\Delta V_{i_a,j} & \text{if } i = i_a,\\ 0 & \text{otherwise.}\end{cases} \tag{3.4}$$

Collecting all cell values into a global vector $\boldsymbol{S}$, we obtain the semi-discrete system in matrix form

$$\frac{\mathrm{d}\boldsymbol{S}}{\mathrm{d}t} = \boldsymbol{D}_S^n\boldsymbol{S} + \boldsymbol{R}_S(\boldsymbol{S},\boldsymbol{B}) + \boldsymbol{E}^n,$$

where $\boldsymbol{D}_S^n \in \mathbb{R}^{N\times N}$ $(N = N_rN_z)$ is the sparse, banded diffusion matrix assembled from the coefficients in (3.2) (for $i \neq i_a$) and (3.3) (for $i = i_a$).

3.3. **Semi-discrete scheme for the bacteria equation.** The bacterial equation (2.4b) contains both a diffusive flux $\sigma\nabla B$ and a chemotactic (advective) flux $\chi B\nabla S$. The diffusive term is discretized identically to (3.2) with D replaced by σ. For the chemotactic term, the advective velocity at each cell interface is computed from the substrate gradient by centered differences:

$$v_{r,i+1/2,j} = \chi\frac{S_{i+1,j}-S_{i,j}}{\Delta r}, \quad v_{z,i,j+1/2} = \chi\frac{S_{i,j+1}-S_{i,j}}{\Delta z}, \tag{3.5}$$

and similarly at the remaining interfaces. The flux of the bacterial concentration at each interface is then reconstructed by the first-order upwind rule, which we describe by introducing the standard upwind operator $\mathrm{Upw}(\cdot;\cdot,\cdot)$ (cf., e.g., [42]). If for $a \in \mathbb{R}$ we define $a^+ \coloneqq \max\{a,0\}$ and $a^- \coloneqq \min\{a,0\}$, then this operator is defined by

$$\mathrm{Upw}(a;b,c) \coloneqq a^+b + a^-c.$$

This upwind choice preserves positivity of B and suppresses oscillations near sharp chemotactic fronts [33]. Similarly to the derivation of (3.2) we now obtain

$$\begin{aligned}\frac{\mathrm{d}B_{i,j}}{\mathrm{d}t} = {}& \frac{\sigma}{\Delta V_{i,j}}\Bigg\{\frac{B_{i-1,j}-B_{i,j}}{\Delta r}A_{r,i-1/2} - \frac{B_{i,j}-B_{i+1,j}}{\Delta r}A_{r,i+1/2}\\ &\qquad + \frac{B_{i,j-1}-B_{i,j}}{\Delta z}A_{z,i} - \frac{B_{i,j}-B_{i,j+1}}{\Delta z}A_{z,i}\Bigg\}\\ &+ \frac{1}{V_{i,j}}\big(\mathrm{Upw}(v_{r,i-1/2,j};B_{i-1,j},B_{i,j})A_{r,i-1/2} - \mathrm{Upw}(v_{r,i+1/2,j};B_{i,j},B_{i+1,j})A_{r,i+1/2}\\ &\qquad \mathrm{Upw}(v_{z,i,j-1/2};B_{i,j-1},B_{i,j})A_{z,j-1/2} - \mathrm{Upw}(v_{z,i,j+1/2};B_{i,j},B_{i,j+1})A_{z,j+1/2}\big)\\ &+ R_B(S_{i,j},B_{i,j}).\end{aligned} \tag{3.6}$$

Notice that (3.6) corresponds to an interior point indexed by (i,j) not affected by zero-flux boundary conditions. If the stencil centered at (i,j) involves differences to neighboring points subject to a discretized version of the zero-flux boundary condition (2.7), then the corresponding difference within the term in curled brackets and the corresponding upwind flux are set to zero. Summarizing all ingredients we may assemble the resulting semi-discrete system for all cell values into $\boldsymbol{B}$ reads

$$\frac{\mathrm{d}\boldsymbol{B}}{\mathrm{d}t} = \boldsymbol{D}_B^n\boldsymbol{B} + \boldsymbol{U}(\boldsymbol{S})\boldsymbol{B} + \boldsymbol{R}_B(\boldsymbol{S},\boldsymbol{B}), \tag{3.7}$$

where $\boldsymbol{D}_B$ is the diffusion/motility matrix, $\boldsymbol{U}(\boldsymbol{S})$ is the "upwind matrix" that collects the coefficients defined by eq:vridef–eq:upwind (that multiply the B-values), and $\boldsymbol{R}_B$ is the reaction vector.

3.4. **Moving-boundary correction.** At each time step t_n the root tip position L_{R}^n determines the cut cell $\bar{j}^n$ and fraction α^n (Section 2). The effective volume and radial interface areas of every cell in the cut row are scaled by α^n, i.e., we define the corrected quantities

$$\overline{\Delta V}_{i,j}^n := \begin{cases} \alpha^n \Delta V_{i,j} & \text{if } i < i_a \text{ and } j = \bar{j}^n, \\ \Delta V_{i,j} & \text{otherwise} \end{cases} \quad \text{and}$$

$$\bar{A}_{r,i\pm1/2}^n := \begin{cases} \alpha^n A_{r,i\pm1/2} & \text{if } i = i_a \text{ and } j = \bar{j}^n, \\ A_{r,i\pm1/2}, & \text{otherwise} \end{cases}$$

that replace $\Delta V_{i,j}$ and $A_{r,i\pm1/2}$, respectively, in equations (3.2)–(3.7) for the affected cells. Diffusion is set to zero inside $\Omega_{\mathrm{R}}(t)$ by means of a binary mask. Whenever $\bar{j}^{n+1} \neq \bar{j}^n$ (i.e. the root tip crosses a cell boundary), the matrices $\boldsymbol{D}_S$, $\boldsymbol{D}_B$ and $\boldsymbol{U}$ are reassembled and refactored.

3.5. **Fully discrete numerical scheme.** We introduce a fully discrete numerical scheme for the approximate solution of the semi-discrete scheme and suppose we wish to advance the solution by one time step from t_n to $t_{n+1} = t_n + \Delta t$. The fully discrete scheme should have the following properties: the scheme should be easy to execute in the sense that the scheme is either explicit or in each time step, at most linear (but no nonlinear) systems need to be solved; in the latter case the time step should be bounded by a Courant-Friedrichs-Lewy (CFL) condition (see below); and the scheme should be positivity preserving: if $\boldsymbol{S}^n$ and $\boldsymbol{B}^n$ denote the vectors of approximate values $S_{i,j}^n \approx S_{i,j}(t_n)$ and $B_{i,j}^n \approx B_{i,j}(t_n)$ and we assume that

$$S_{i,j}^n \geq 0 \quad \text{and} \quad B_{i,j}^n \geq 0 \quad \text{for all indices } i \text{ and } j, \tag{3.8}$$

then it must be ensured that the same property (3.8) also holds for $S_{i,j}^{n+1}$ and $B_{i,j}^{n+1}$ for all i and j.

We here propose a splitting method as a numerical algorithm for the computation of $\boldsymbol{S}^{n+1}$ and $\boldsymbol{B}^{n+1}$ from $\boldsymbol{S}^n$ and $\boldsymbol{B}^n$ that proceeds in the following four steps, where we assume that given spatial meshwidths Δz and Δr the time step Δt is chosen such that the CFL condition

$$\Delta t \leq \begin{cases} 1/\mu_{\max} & \text{if } \theta = 1, \\ \min\left\{ \dfrac{1}{\mu_{\max}}, \dfrac{\alpha_{\min}}{2D(1-\theta)\left(\frac{1}{\Delta r^2} + \frac{1}{\Delta z^2}\right)} \right\} & \text{if } 0 \leq \theta < 1 \end{cases} \tag{3.9}$$

is satisfied:

(1) For all indices (i,j), we compute an intermediate value $B_{i,j}^{n+1/2}$ by the explicit discretization

$$B_{i,j}^{n+1/2} = B_{i,j}^n + \Delta t R_B\big(S_{i,j}^n, B_{i,j}^n\big) = \big(1 - \Delta t\big(\mu\big(S_{i,j}^n\big) - \delta\big)\big) B_{i,j}^n \tag{3.10}$$

of the reaction equation $\mathrm{d}\boldsymbol{B}/\mathrm{d}t = \boldsymbol{R}_B(\boldsymbol{S}, \boldsymbol{B})$.

(2) For all indices (i,j), we compute an intermediate value $S_{i,j}^{n+1/2}$ by the implicit discretization

$$\begin{aligned} S_{i,j}^{n+1/2} &= S_{i,j}^n + \Delta t R_S\big(S_{i,j}^{n+1/2}, B_{i,j}^n\big) \\ &= S_{i,j}^n - \Delta t \left(\frac{\mu(S_{i,j}^{n+1/2})}{Y} + m\big(S_{i,j}^{n+1/2}\big) \right) B_{i,j}^n \end{aligned} \tag{3.11}$$

of the reaction equation $\mathrm{d}\boldsymbol{S}/\mathrm{d}t = \boldsymbol{R}_S(\boldsymbol{S}, \boldsymbol{B})$.

(3) We compute the final values $S_{i,j}^{n+1}$ contained in $\boldsymbol{S}^{n+1}$ by solving the linear system

$$\big(\boldsymbol{I}-\theta\Delta t\boldsymbol{D}_S^{n+1}\big)\boldsymbol{S}^{n+1}=\big(\boldsymbol{I}+(1-\theta)\Delta t\boldsymbol{D}_S^{n}\big)\boldsymbol{S}^{n+1/2}+\Delta t\boldsymbol{E}^{n}. \tag{3.12}$$

(4) We compute the final values $B_{i,j}^{n+1}$ contained in $\boldsymbol{B}^{n+1}$ by solving the linear system

$$\big(\boldsymbol{I}-\Delta t\big(\boldsymbol{D}_B^{n+1}+\boldsymbol{U}(\boldsymbol{S}^{n+1})\big)\big)\boldsymbol{B}^{n+1}=\boldsymbol{B}^{n+1/2}. \tag{3.13}$$

Lemma 3.1. *Assume that the CFL condition (3.9) is in effect. Then* $B_{i,j}^{n+1/2}\geq 0$.

Proof. Noticing that $\mu(S)<\mu_{\max}$ for all $S\geq 0$ we obtain that by the CFL condition,

$$1-\Delta t\big(\mu\big(S_{i,j}^{n}\big)-\delta\big)\geq 1-\Delta t\mu_{\max}\geq 0,$$

hence (3.10) implies that $B_{i,j}^{n+1/2}\geq 0$. □

Lemma 3.2.

(i) *For any function $\mu=\mu(S)$ that is continuous, piecewise differentiable, and non-decreasing such that $\mu(0)=0$ and $\mu'(S)\geq 0$ for almost all $S\geq 0$, for each $\Delta t\geq 0$ equation (3.11) has a unique solution $S_{i,j}^{n+1/2}\geq 0$.*

(ii) *For $B\geq 0$ we define the function*

$$G(S)\coloneqq S+\Delta t\left(\frac{\mu(S)}{Y}+m(S)\right)B. \tag{3.14}$$

If $\mu(S)$ is given as the Monod growth rate function (1.2) and we set $B\coloneqq B_{i,j}^{n+1/2}$ and $\tilde{S}\coloneqq S_{i,j}^{n}$, then if $G(m_0/\kappa_0)\leq\tilde{S}$ (Case 1), we get

$$S_{i,j}^{n+1/2}=-\frac{1}{2}\left(\beta+\frac{\alpha-\tilde{S}}{1+\gamma}\right)+\left(\frac{\beta\tilde{S}}{1+\gamma}+\frac{1}{4}\left(\frac{\alpha-\tilde{S}}{1+\gamma}\right)^2\right)^{1/2},$$

where we define $\alpha\coloneqq B\Delta t\mu_{\max}/Y$, $\beta\coloneqq\rho K_S$ and $\gamma\coloneqq B\Delta t\kappa$. On the other hand, if $G(m_0/\kappa_0)>\tilde{S}$ (Case 2), then

$$S_{i,j}^{n+1/2}=\frac{1}{2}(\alpha+\beta+\tilde{\gamma}-\tilde{S})+\left(\beta(\tilde{S}-\tilde{\gamma})+\frac{1}{4}(\alpha+\beta+\tilde{\gamma}-\tilde{S})^2\right)^{1/2},$$

with α and β as defined in Case 1 and $\tilde{\gamma}\coloneqq B\Delta t m_0$.

Proof. To prove part (i), consider the function $G(s)$ defined in (3.14). Clearly, wherever the derivative $G'(s)$ is defined, there holds

$$G'(S)=1+B\Delta t\left(\frac{\mu'(S)}{Y}+m'(S)\right)>0,$$

so G is a strictly increasing function of S. Moreover, for any fixed values of Δt and B there holds $G(0)=0$ (by the properties on $\mu(S)$ and $m(S)$), along with $G(S)\to\infty$ as $S\to\infty$. Consequently, equation (3.11), written as

$$G\big(S_{i,j}^{n+1/2}\big)=S_{i,j}^{n}, \tag{3.15}$$

has a unique non-negative solution, which concludes the proof of (i). The assertions of (ii) are a consequence of (i) if we take into account that G changes its algebraic definition across m_0/κ and that in the case of the Monod kinetics (1.2), (3.15) is a quadratic equation. □

In view of Lemmas 3.1 and 3.2 we may assert that if $\boldsymbol{S}^n\geq\boldsymbol{0}$ and $\boldsymbol{B}^n\geq\boldsymbol{0}$ then there also hold $\boldsymbol{S}^{n+1/2}\geq\boldsymbol{0}$ and $\boldsymbol{B}^{n+1/2}\geq\boldsymbol{0}$.

Lemma 3.3. *For all $\theta \in [0,1]$ the matrix $\boldsymbol{M} \coloneqq \boldsymbol{I} - \theta\Delta t \boldsymbol{D}_S^{n+1}$ on the left-hand side of (3.12) is an M-matrix, which means that is inverse exists and is non-negative, i.e., $\boldsymbol{M}^{-1} \geq \boldsymbol{0}$ (understood in the entry-wise sense). Moreover, if the CFL condition (3.9) is in effect, then the matrix $\boldsymbol{N} \coloneqq \boldsymbol{I} + (1-\theta)\Delta t \boldsymbol{D}_S^n$ is nonnegative, i.e., $\boldsymbol{N} \geq \boldsymbol{0}$.*

Proof. For $\theta = 0$ there holds $\boldsymbol{M} = \boldsymbol{I}$ and there is nothing to prove. On the other hand, assume that the entries of $\boldsymbol{D}_S^{n+1}$ are denoted by $(d_S^{n+1})_{(i,j),(k,l)}$. Assume (for simplicity) that the boundary conditions are not involved for the computation of $S_{i,j}^{n+1}$. Then the diagonal entry of row (i,j) is

$$(d_S^{n+1})_{(i,j),(i,j)} = -\frac{D}{\overline{\Delta V}_{i,j}^{n+1}}\left(\frac{\bar{A}_{r,i-1/2}^{n+1} + \bar{A}_{r,i+1/2}^{n+1}}{\Delta r} + \frac{2A_{z,i}}{\Delta z}\right) < 0.$$

All other entries in that row are zero, with the exception of

$$(d_S^{n+1})_{(i,j),(i\pm1,j)} = \frac{D\bar{A}_{r,i\pm1/2}^{n+1}}{\overline{\Delta V}_{i,j}^{n+1}\Delta r} > 0, \quad (d_S^{n+1})_{(i,j),(i,j\pm1)} = \frac{DA_{z,i}}{\overline{\Delta V}_{i,j}^{n+1}\Delta z} > 0.$$

Taking into account that similar reasoning applies to those rows that are affected by the zero-flux boundary conditions (2.6), which are implemented by setting corresponding S-differences to zero, and similarly in cases when (3.2) is replaced by (3.3), we obtain that the diagonal entries of $\boldsymbol{M}$ are positive while the off-diagonal entries are non-positive, hence $\boldsymbol{M}$ has the sign structure of an L-matrix. Moreover, $\boldsymbol{M}$ is strictly diagonally dominant for all choices of θ and Δt. Therefore $\boldsymbol{M}$ is indeed an M-matrix. On the other hand, for $\theta = 1$ we trivially have $\boldsymbol{N} = \boldsymbol{I} \geq 0$. For $0 \leq \theta < 1$ we take into account that the off-diagonal entries of $\boldsymbol{N}$ are always non-negative. The diagonal entries are nonnegative provided that

$$1 + (1-\theta)\Delta t (d_S^n)_{(i,j),(i,j)} \geq 0 \quad \text{for all } (i,j). \tag{3.16}$$

Taking into account that by (3.1),

$$\left|(d_S^n)_{(i,j),(i,j)}\right| \leq \frac{D}{\alpha_{\min} r_i \Delta z \Delta r}\left(\frac{r_{i-1/2} + r_{i+1/2}}{\Delta r}\Delta z + \frac{2r_i\Delta r}{\Delta z}\right) = \frac{2D}{\alpha_{\min}}\left(\frac{1}{\Delta r^2} + \frac{1}{\Delta z^2}\right),$$

a sufficient condition for (3.16) to hold is

$$\frac{2D\Delta t}{\alpha_{\min}}\left(\frac{1}{\Delta r^2} + \frac{1}{\Delta z^2}\right) \leq \frac{1}{1-\theta}. \tag{3.17}$$

Inequality (3.17) holds, however, when the CFL condition is in effect. □

Lemma 3.4. *Assume that the CFL condition (3.9) is in effect and that $\boldsymbol{S}^{n+1}$ is computed from $\boldsymbol{S}^{n+1/2}$ by solving the linear system (3.12). Then $\boldsymbol{S}^{n+1} \geq \boldsymbol{0}$.*

Proof. Lemma 3.1 implies that $(\boldsymbol{I} + (1-\theta)\Delta t \boldsymbol{D}_S^n)\boldsymbol{S}^{n+1/2} \geq \boldsymbol{0}$. On the other hand, from (3.4) we deduce that $\boldsymbol{E}^n \geq \boldsymbol{0}$. Thus, multiplying (3.12) from the left by $\boldsymbol{M}^{-1} = (\boldsymbol{I} - \theta\Delta t \boldsymbol{D}_S^{n+1})^{-1} \geq \boldsymbol{0}$, we get

$$\boldsymbol{S}^{n+1} = \left(\boldsymbol{I} - \theta\Delta t \boldsymbol{D}_S^{n+1}\right)^{-1}\left(\left(\boldsymbol{I} + (1-\theta)\Delta t \boldsymbol{D}_S^n\right)\boldsymbol{S}^{n+1/2} + \Delta t \boldsymbol{E}^n\right) \geq \boldsymbol{0}.$$

□

Lemma 3.5. *The matrix $\boldsymbol{J} \coloneqq \boldsymbol{I} - \theta\Delta t(\boldsymbol{D}_B^{n+1} + \boldsymbol{U}(\boldsymbol{S}^{n+1}))$ on the left-hand side of (3.13) is an M-matrix, which means that is inverse exists and is non-negative, i.e., $\boldsymbol{J}^{-1} \geq \boldsymbol{0}$ (understood in the entry-wise sense).*

Proof. By following the proof of Lemma 3.3, with obvious replacements, we obtain that $\boldsymbol{I} - \Delta t \boldsymbol{D}_B^{n+1}$ is a diagonally dominant L-matrix and therefore an M-matrix. Let us denote the entries of $\boldsymbol{U}(\boldsymbol{S}^{n+1})$ by $u^{n+1}_{(i,j)(k,l)}$, and assume that the velocities $v^{n+1}_{r,i+1/2,j}$ and $v^{n+1}_{r,i,j+1/2}$ are computed as in (3.5) with all values $S_{i,j}$ replaced by $S^{n+1}_{i,j}$. In view of (3.6), and for the moment considering an interior point not influenced by boundary conditions, we get

$$u^{n+1}_{(i,j)(i,j)} = \frac{1}{\bar{V}^{n+1}_{i,j}}\big(-v^{n+1,+}_{r,i-1/2,j}\bar{A}^{n+1}_{r,i-1/2,j} + v^{n+1,+}_{r,i+1/2,j}\bar{A}^{n+1}_{r,i+1/2,j} - v^{n+1,+}_{z,i,j-1/2}A_{z,i} + v^{n+1,-}_{z,i,j+1/2}A_{z,i}\big) \le 0,$$

$$u^{n+1}_{(i,j)(i+1,j)} = -\frac{v^{n+1,-}_{r,i+1/2,j}\bar{A}^{n+1}_{r,i+1/2}}{\bar{V}^{n+1}_{i,j}} \ge 0, \quad u^{n+1}_{(i,j)(i-1,j)} = \frac{v^{n+1,+}_{r,i-1/2,j}\bar{A}^{n+1}_{r,i-1/2}}{\bar{V}^{n+1}_{i,j}} \ge 0,$$

$$u^{n+1}_{(i,j)(i,j+1)} = -\frac{v^{n+1,-}_{r,i,j+1/2}\bar{A}_{z,i}}{\bar{V}^{n+1}_{i,j}} \ge 0, \quad u^{n+1}_{(i,j)(i,j-1)} = \frac{v^{n+1,+}_{r,i,j-1/2}\bar{A}_{z,i}}{\bar{V}^{n+1}_{i,j}} \ge 0;$$

all other entries in row (i,j) are zero. The inequalities remain valid in case that boundary conditions need to be incorporated, with the effect that one or several "Upw(...)" expressions in (3.6), and correspondingly in the fully discrete formulation need to be replaced by zero. Consequently, $-\Delta t\boldsymbol{U}(\boldsymbol{S}^{n+1})$ is an L-matrix, and in each row its diagonal entry and the sum of off-diagonal entries exactly cancel. We therefore conclude that $\boldsymbol{J}$ is a strictly diagonally dominant L-matrix, and therefore an M-matrix. □

Finally, we comment that Lemmas 3.1 to 3.5 and their proofs provide a proof of the following theorem.

Theorem 3.1. *Assume that the CFL condition (3.9) is in effect. Then the numerical scheme described by steps (1) to (4) is positivity preserving, i.e., if $\boldsymbol{S}^n \ge \boldsymbol{0}$ and $\boldsymbol{B}^n \ge \boldsymbol{0}$ then it follows that $\boldsymbol{S}^{n+1} \ge \boldsymbol{0}$ and $\boldsymbol{B}^{n+1} \ge \boldsymbol{0}$.*

To justify the present approach, let us comment that the only part of the system (2.4) that can be handled by an explicit method is the reaction equation $\mathrm{d}\boldsymbol{B}/\mathrm{d}t = \boldsymbol{R}_B(\boldsymbol{S},\boldsymbol{B})$, as is done in Step 1 above. For the further procedure one should keep in mind that due to the particular structure of the chemotactic term in (1.1b) or (2.4b), which introduces cross-diffusion, solution values of B may become arbitrarily large within finite time (the so-called blow-up phenomenon). This is a well-known property of the Keller-Segel system [24]; see for instance [25]. In princple, $B_{i,j}$ can become arbitrarily large, which motivates our choice of an implicit method to handle of the reaction equation $\mathrm{d}\boldsymbol{S}/\mathrm{d}t = \boldsymbol{R}_S(\boldsymbol{S},\boldsymbol{B})$: Step 2 is taken in implicit form since an a priori upper bound of $B^n_{i,j}$ is not available. Next, in Step 3, we deal with the diffusive part of (1.1a) or (2.4a), for which a θ-method can be employed. Notice, however, that for $\theta \in [0,1)$ the CFL condition (3.9) is much less favorable than for $\theta = 1$; in particular, for $\theta \in [0,1)$ there is a sensitive dependence on the parameter $\alpha_{\min}$. Finally, with respect to Step 4, we recall that the transport velocity in the chemotactical term, that is the gradient ∇S, and its discrete analogue can become arbitrarily large; it would be difficult to find conditions on Δt to guarantee preservation of positivity if we had chosen an explicit or θ-scheme with $\theta \in [0,1)$, similar to (3.13), instead of (3.12) for that step.

4. Numerical results

The results presented in this section, organized as "examples," were obtained by implementing the numerical scheme described in Section 3 using parameters drawn from the literature. Two stages are considered: first, a one-dimensional validation against the classical Newman–Watson

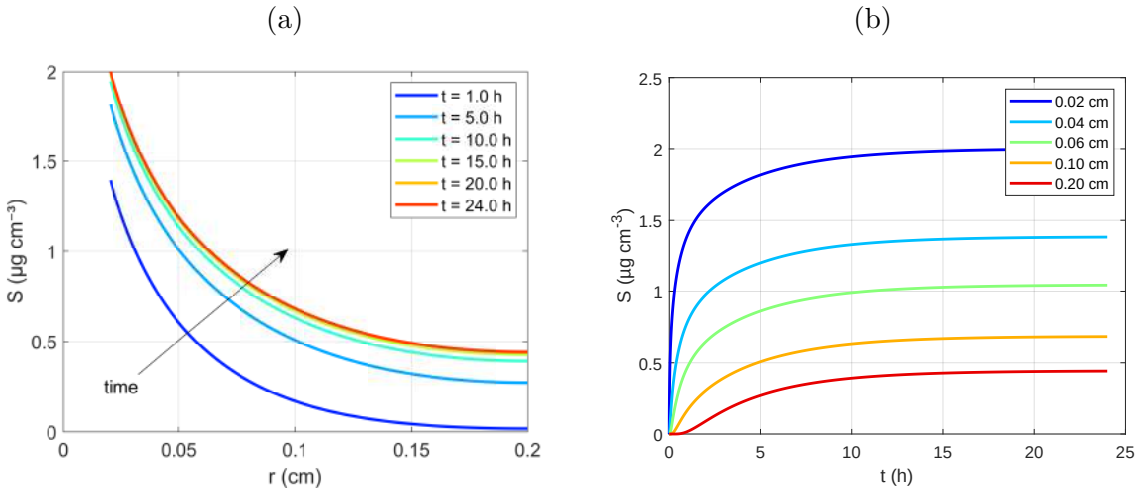

FIGURE 3. Example 1 (one-dimensional Newman–Watson model): (a) radial concentration profiles of substrate S ($N = 800$) at successive times; colors indicate increasing time, (b) temporal evolution of substrate concentration at different radial positions; steady state is established between 10 h and 15 h.

model [16]; second, a series of two-dimensional parametric scenarios using the complete coupled system.

4.1. **Example 1: one-dimensional Newman–Watson model.** To validate the spatial discretization, the one-dimensional, steady-state substrate model of [16] was reproduced without coupling to a bacterial population. The domain spans the radial interval $[a, b] = [0.02\,\text{cm}, 0.2\,\text{cm}]$ with diffusion coefficient $D = 3.6 \times 10^{-3}\,\text{cm}^2\,\text{h}^{-1}$, maximum specific uptake rate $\mu_{\max}/Y = 0.4\,\text{h}^{-1}$, saturation constant $K_s = 10\,\mu\text{g}\,\text{cm}^{-3}$, constant exudation flux $Q = 0.167\,\mu\text{g}\,\text{cm}^{-2}\,\text{h}^{-1}$, maintenance coefficient $C = 0$, water content of soil $\rho = 0.3$ and initial substrate concentration $S_0 = 0$. The simulated time is 24 h, using a cell-centered finite volume mesh with $N = 800$ control volumes. The computed profiles (see Figure 3(a)) reproduce those reported by [16]: the substrate concentration is highest at the root surface and decreases outward, with a maximum value of $2.0\,\mu\text{g}\,\text{cm}^{-3}$. The system reaches steady state at approximately 10 h of simulation, in agreement with the reference result (Figure 3(b)). This consistency confirms that the FVM discretization in cylindrical coordinates is correct before we proceed to the fully coupled two-dimensional model.

4.2. **Examples 2 to 9: two-dimensional simulations.** The complete coupled model was simulated over 30 days (720 h) on a 200×200 mesh with time step $\Delta t = 0.5\,\text{h}$ and $\theta = 1$. The model parameters, taken from the literature and calibrated as described below, are summarized in Table 2. This set defines the base scenario of Example 2. The remaining examples are constructed cumulatively: each one modifies a single parameter while retaining the changes introduced in the previous examples. The root-growth parameters l and β were calibrated using the experimental data of [46], which report root depths of 15–20 cm over 30 days of cultivation; an asymptotic length $l = 25\,\text{cm}$ was chosen to ensure biologically consistent behavior throughout the simulation period. The exudation parameters $Q_{\text{m}} = 0.66\,\mu\text{g}\,\text{cm}^{-2}\,\text{h}^{-1}$ and $d = 0.003\,\text{h}^{-1}$ were determined from the total organic carbon rates and temporal profiles reported for rice (*Oryza sativa* L.) by Schwalm et al. [41, 47].

TABLE 2. Parameters used in the 2D simulations.

Symbol	Description	Value	Reference
S_0	Substrate (exudate) concentration [$\mu g\,cm^{-3}$]	0	[16]
B_0	Bacterial biomass concentration [$\mu g\,cm^{-3}$]	0	[16]
D	Substrate diffusion coefficient [$cm^2\,h^{-1}$]	10^{-5}	[16, 29]
σ	Bacterial motility coefficient [$cm^2\,h^{-1}$]	0	[29, 43]
χ	Chemotactic sensitivity [$cm^5\,\mu g^{-1}\,h^{-1}$]	0	[29]
κ	Parameter in maintenance rate function	100	—
$\mu_{\max}$	Maximum specific growth rate [h^{-1}]	0	[16, 29]
K_s	Half-saturation constant [$\mu g\,cm^{-3}$]	70	[16, 29]
ρ	Substrate bioavailability factor (dimensionless)	0.3	[44, 45]
Y	Yield coefficient (dimensionless)	0.4	[16, 45]
m_0	Cell maintenance rate constant [h^{-1}]	0	[16]
δ	Bacterial decay rate [h^{-1}]	0	[29]
l	Asymptotic root length [cm]	25	[46]
β	Root elongation rate [h^{-1}]	0.001	[46]
Q_{m}	Maximum exudation rate [$\mu g\,cm^{-2}\,h^{-1}$]	0.66	[41, 47]
d	Exudation decay rate [h^{-1}]	0.003	[41, 47]
a	Root radius [cm]	0.02	[48, 49]
b	Rhizosphere radius [cm]	0.45	[50, 51]

4.2.1. *Example 2: substrate dynamics without bacteria.* In this example, all biological parameters were set to zero to observe the substrate in isolation. The simulation produces a sharp gradient with the highest substrate accumulation at the root surface (Figure 4), reproducing the accumulation zones described by [18]: just as roots generate depletion zones when absorbing nutrients, exudate release creates accumulation zones around the root. A maximum substrate concentration of $1129\,\mu g\,cm^{-3}$ was recorded. This confirms that, without microbial consumption, continuous exudation leads to a substrate-rich environment whose distribution is governed solely by diffusion.

4.2.2. *Example 3: influence of bacterial biomass.* In Example 3, bacterial dynamics were included but chemotaxis was suppressed ($\chi = 0$). The growth, decay, and maintenance rates were set to $\mu_{\max} = 0.165\,h^{-1}$, $\delta = 0.012\,h^{-1}$ and $m_0 = 0.02\,h^{-1}$, with isotropic motility $\sigma = 10^{-5}\,cm^2\,h^{-1}$, and initial biomass $B_0 = 10^{-3}\,\mu g\,cm^{-3}$. The maximum substrate concentration was $1114\,\mu g\,cm^{-3}$ and the peak biomass reached $481.4\,\mu g\,cm^{-3}$. Starting from day 6 (144 h), substrate depletion is visible in the older root sections (Figure 5, top), remaining available only in the most recently formed zones, a direct result of bacterial metabolic activity. The corresponding biomass gradient (Figure 5, bottom) consolidates precisely in those regions where substrate has become scarce. This demonstrates that local metabolic consumption drives the substrate depletion, establishing a competitive environment even without directed bacterial movement.

4.2.3. *Example 4: effect of bacterial motility.* Increasing the bacterial motility coefficient from 10^{-5} to $\sigma = 3.0 \times 10^{-3}\,cm^2\,h^{-1}$ enhances the spatial dispersion of the microbial population throughout the rhizosphere. Since the movement remains purely diffusive (i.e., $\chi = 0$), bacteria accumulate in the oldest root sections and are unable to track the advancing root tip. As a consequence, a considerable fraction of substrate remains unconsumed in the deeper zones, as illustrated in

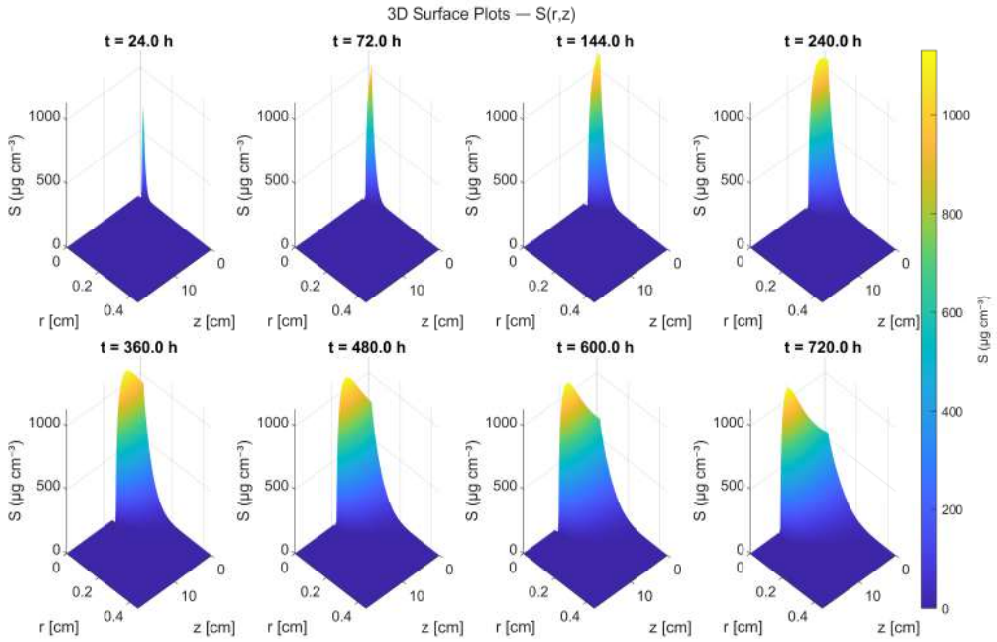

FIGURE 4. Example 2 (substrate dynamics without bacteria): simulated concentration of substrate S without bacterial activity ($\mu_{\max} = \delta = m_0 = \sigma = \chi = B_0 = 0$, Table 2) at eight time instants.

Figure 6 (top). By contrast, Figure 6 (bottom) shows that, by the end of the simulation period, the biomass exhibits a pronounced but broadly distributed radial gradient. This wide dispersion, however, proves inefficient for axial colonization along the root, confirming that random motility alone is insufficient to sustain a spatially coherent colonization front in the presence of a growing root. The highest substrate concentration recorded was $1129\,\mu g\,cm^{-3}$, while the biomass peaked at $7.8\,\mu g\,cm^{-3}$. This indicates that while increased random motility allows the population to occupy a larger volume, the lack of directional guidance prevents efficient utilization of the most active exudation zones near the growing root tip.

4.2.4. *Example 5: effect of bacterial growth rate.* In the preceding motility scenario, rhizosphere colonization was not achieved until day 25 (600 h). To examine a potentially earlier colonization, $\mu_{\max}$ was increased from $0.165\,h^{-1}$ to $0.30\,h^{-1}$ while all other parameters were kept unchanged. Under this condition, colonization begins at day 15 (360 h) in the upper root region, as shown in Figure 7. We observe that the biomass accumulation is markedly larger than in the previous scenarios. The maximum substrate concentration was $1126\,\mu g\,cm^{-3}$ and peak biomass reached $6.4\,\mu g\,cm^{-3}$. The accelerated metabolic rate enables the bacteria to establish a dense population more rapidly, thereby reducing the spatial extent of the available substrate.

4.2.5. *Example 6: effect of chemotaxis.* Activating a non-zero chemotactic sensitivity ($\chi = 1.5 \times 10^{-6}\,cm^5\,\mu g^{-1}\,h^{-1}$) substantially alters the colonization dynamics compared with the purely diffusive scenarios (Examples 3 and 4). The bacteria acquire the capacity to sense and migrate actively toward zones of higher exudate concentration. This directed response produces a marked spatial asymmetry: biomass concentrates near the root surface and descends along a narrower, more directed trajectory following the substrate gradient (Figure 8). The highest substrate concentration

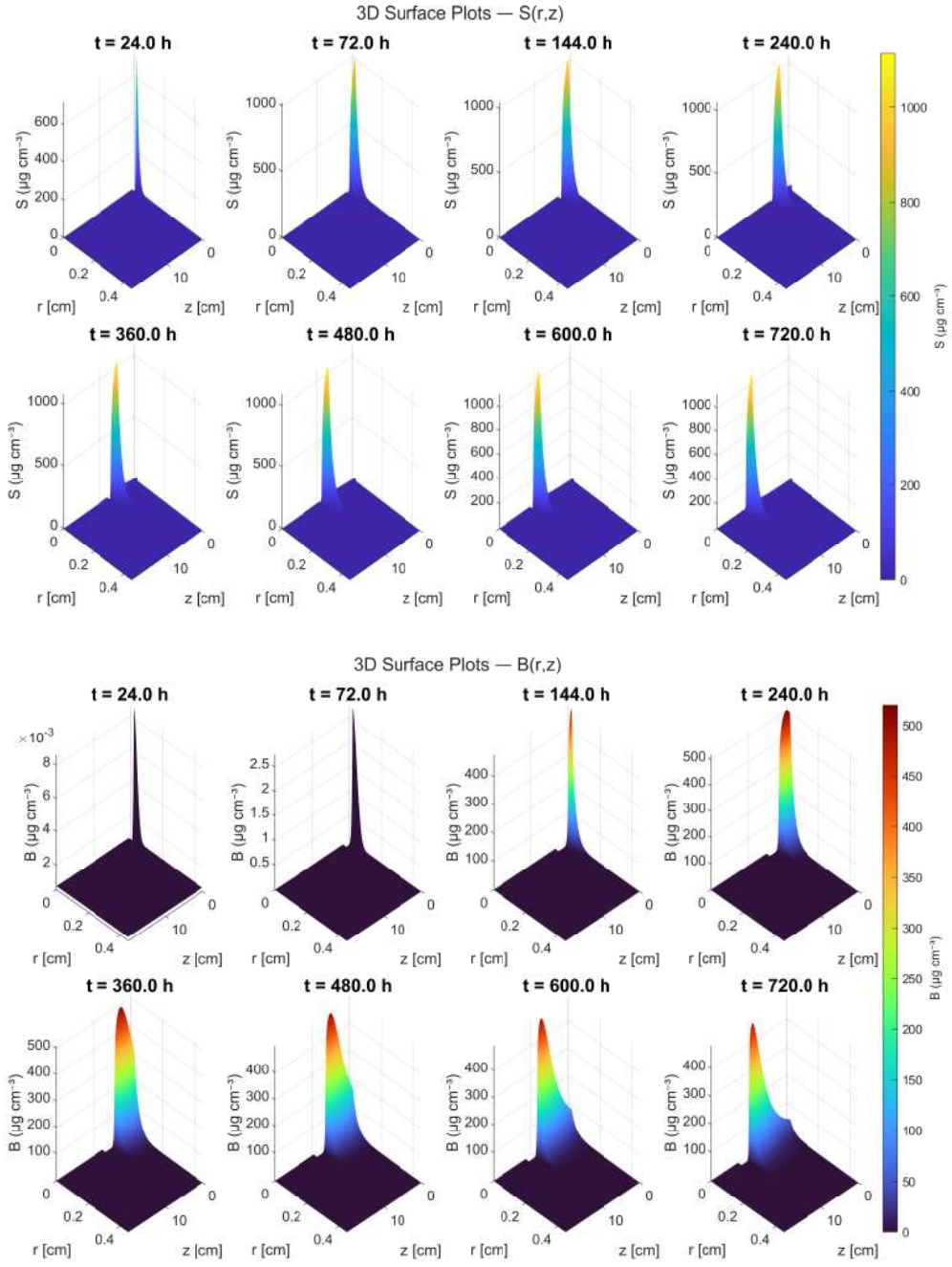

FIGURE 5. Example 3 (influence of bacterial biomass): simulated concentration of (top) substrate S and (bottom) bacterial biomass B without chemotaxis ($\chi = 0$) at eight time instants.

recorded was $1157\,\mu g\,cm^{-3}$, while the biomass peaked at $6.7\,\mu g\,cm^{-3}$. The directed movement ensures that the bacteria actively track the nutrient source, creating a highly localized and efficient colonization front that closely follows the root apex.

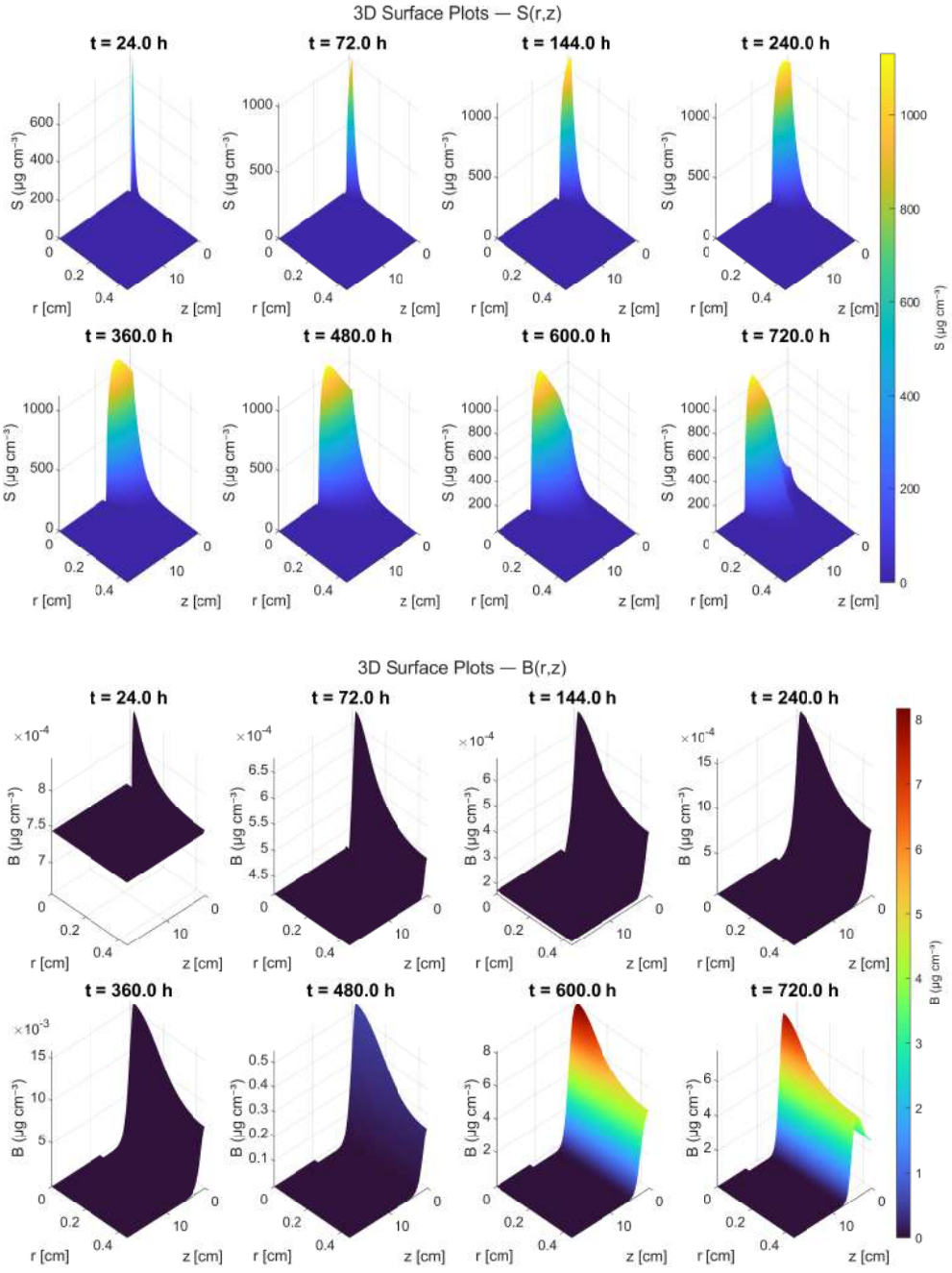

FIGURE 6. Example 4 (effect of bacterial motility): simulated concentration of (top) substrate S and (bottom) bacterial biomass B with enhanced bacterial motility ($\sigma = 3.0 \times 10^{-3}\,\mathrm{cm}^2\,\mathrm{h}^{-1}$) at eight time instants.

The peak bacterial concentration in Figure 8 (bottom) is more intense and spatially localized than in the purely diffusive case, reflecting an efficient response to the chemical gradient. This behavior is consistent with the observations of Dupuy and Silk [29], who show that chemotaxis acts primarily as a radial attraction mechanism toward the nutrient source, narrowing the colonization

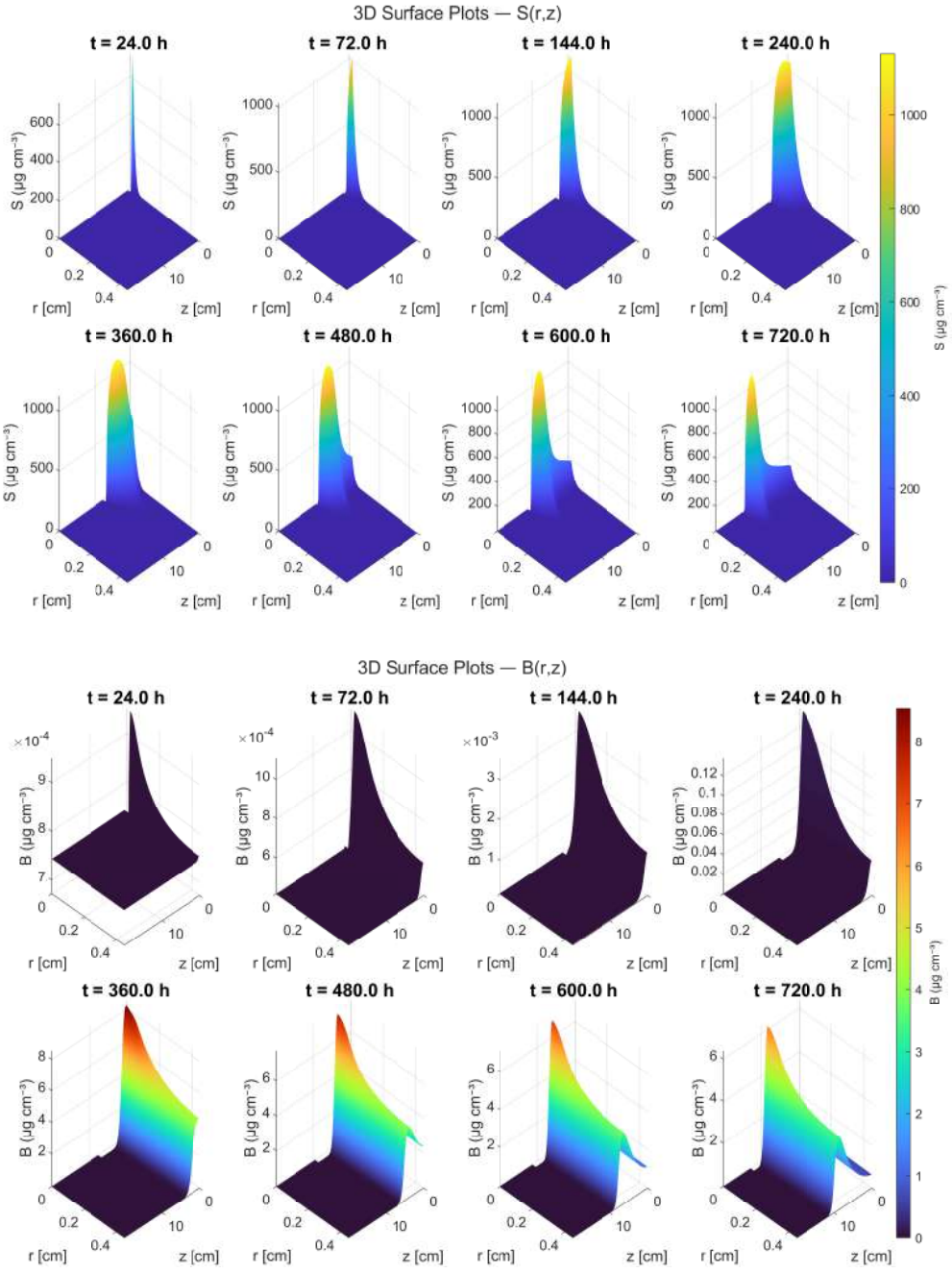

FIGURE 7. Example 5 (effect of bacterial growth rate): simulated concentration of (top) substrate S and (bottom) bacterial biomass B with $\mu_{\max} = 0.30\,\mathrm{h}^{-1}$ at eight time instants.

layer around the root. As those authors note, however, chemotaxis alone cannot compensate for the temporal lag of the population relative to the advancing root tip: axial displacement continues to be governed by the dynamics of root elongation rather than by directed bacterial migration.

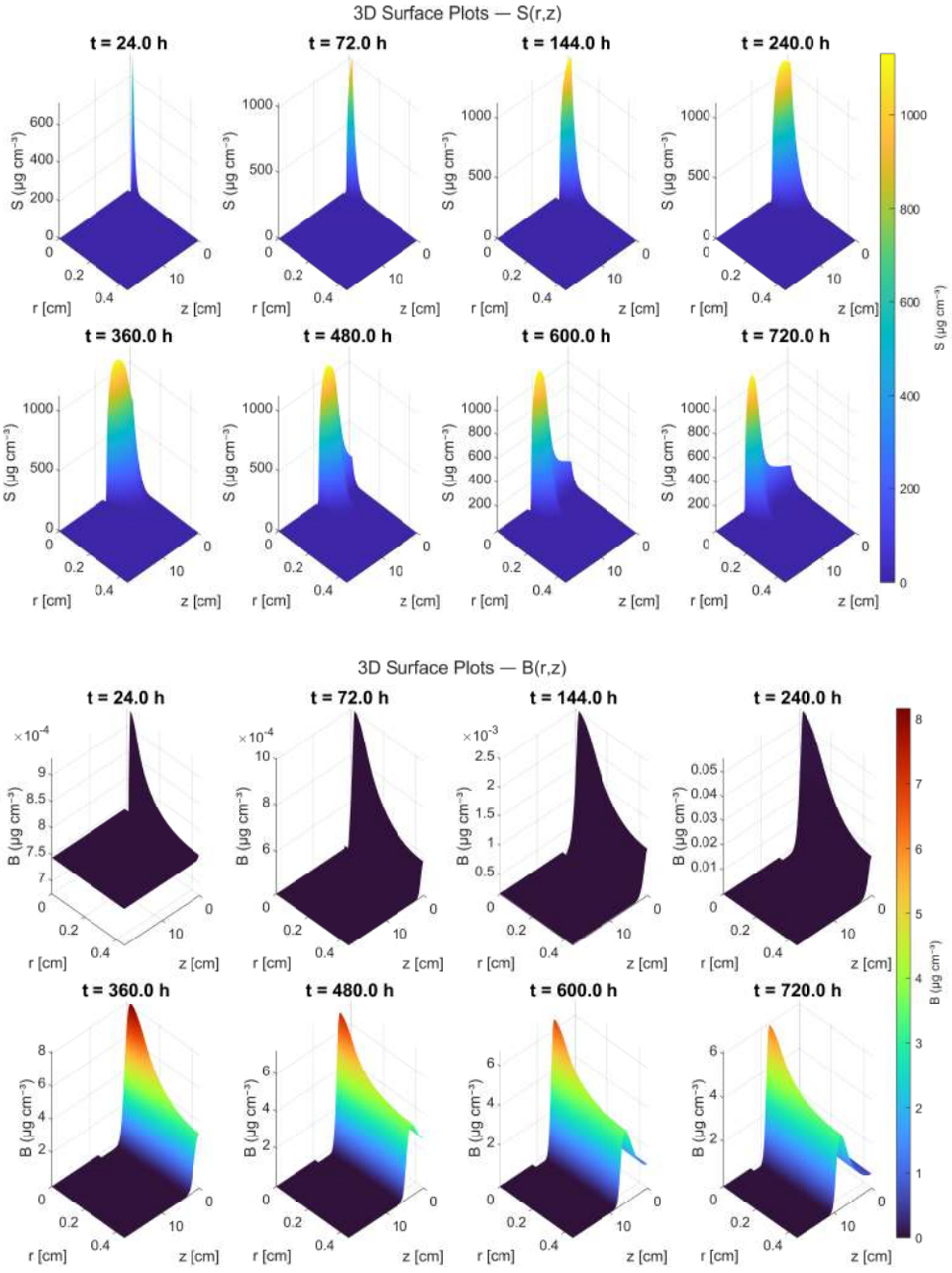

FIGURE 8. Example 6 (effect of chemotaxis): simulated concentration of (top) substrate S and (bottom) bacterial biomass B with active chemotaxis ($\chi = 1.5 \times 10^{-6}\,\mathrm{cm^5\,\mu g^{-1}\,h^{-1}}$) at eight time instants.

4.2.6. *Example 7: effect of higher initial biomass.* Increasing the initial bacterial biomass concentration from 10^{-3} to $B_0 = 2\,\mu\mathrm{g\,cm^{-3}}$ results in an even earlier rhizosphere colonization, as shown in Figure 9. The maximum substrate concentration was $1123\,\mu\mathrm{g\,cm^{-3}}$ and peak biomass reached

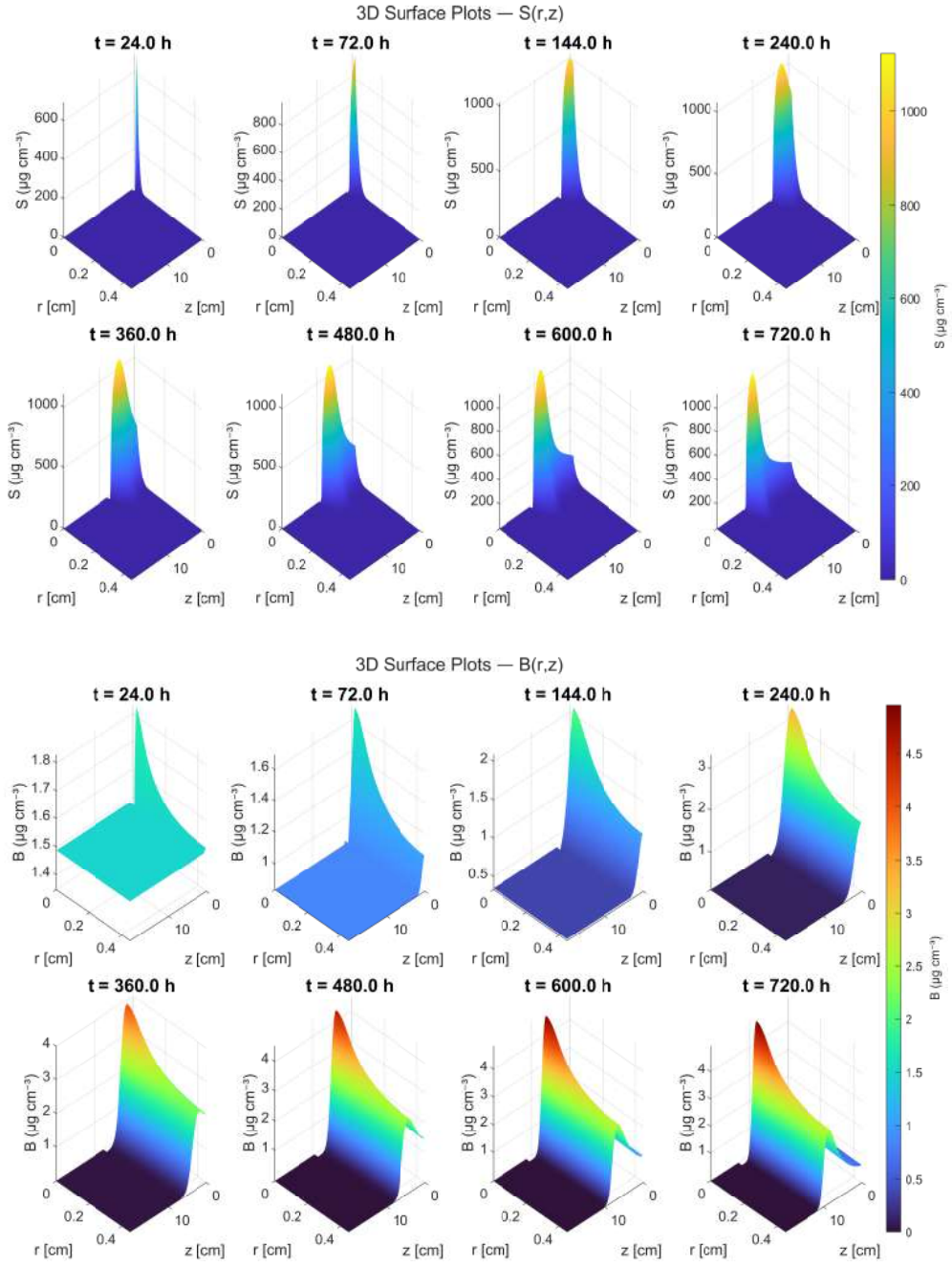

FIGURE 9. Example 7 (effect of higher initial biomass): simulated concentration of (top) substrate S and (bottom) bacterial biomass B with $B_0 = 2\,\mu\mathrm{g\,cm^{-3}}$ at eight time instants.

$4.9\,\mu\mathrm{g\,cm^{-3}}$. A larger initial population accelerates the onset of resource consumption, leading to a faster depletion of exudates and a more uniform early colonization across the available root surface.

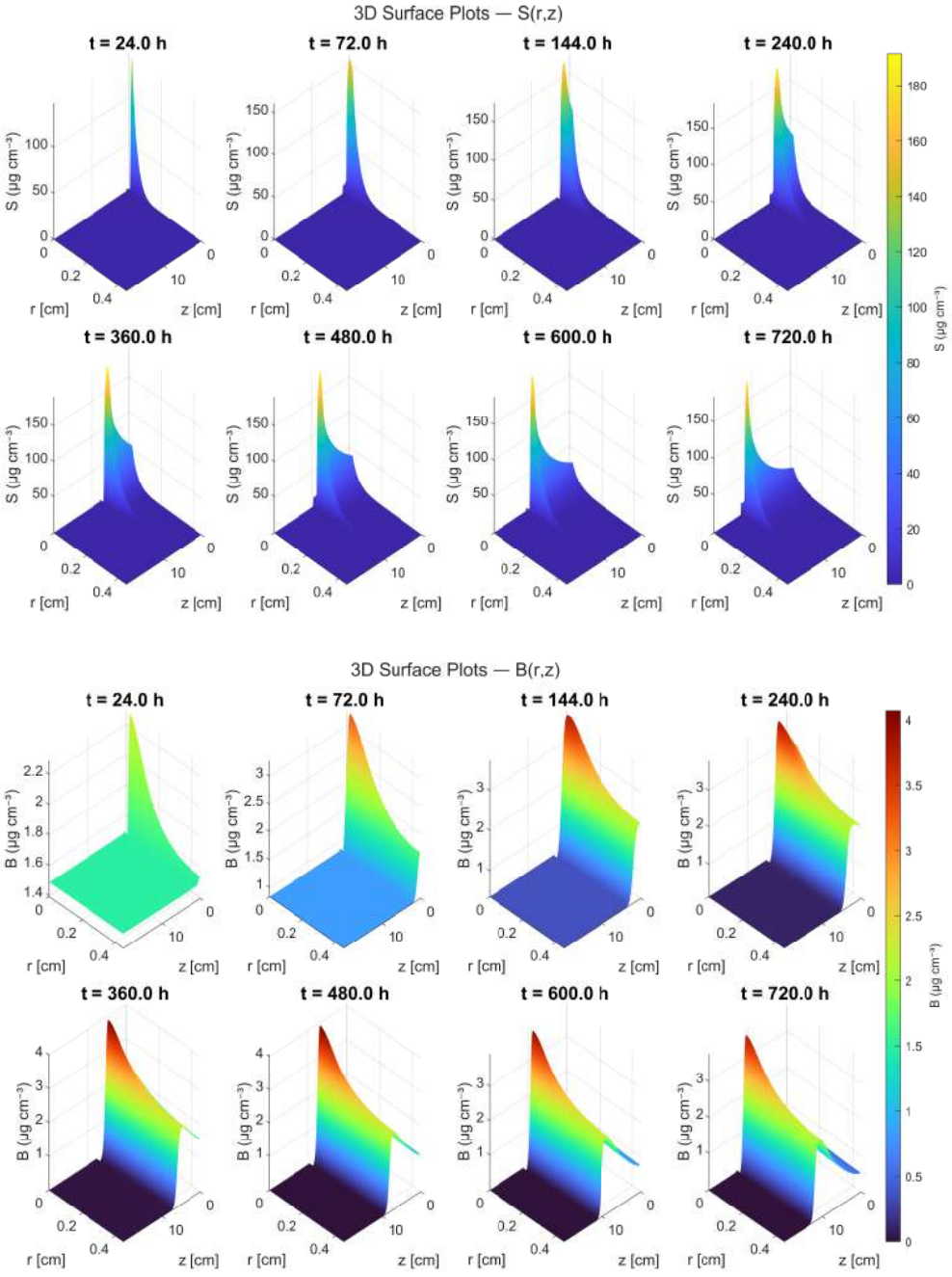

FIGURE 10. Example 8 (effect of increased substrate diffusivity): simulated concentration of (top) substrate S and (bottom) bacterial biomass B with $D = 1.0 \times 10^{-4}\,\mathrm{cm^2\,h^{-1}}$ at eight time instants.

4.2.7. *Example 8: effect of increased substrate diffusivity.* Raising the substrate diffusion coefficient from 10^{-5} to $D = 1.0 \times 10^{-4}\,\mathrm{cm^2\,h^{-1}}$, one order of magnitude above the base value, produces a more extensive and spatially homogeneous distribution of the exudates. As seen in Figure 10, the increased mass-transfer rate results in markedly lower local substrate concentrations, with a

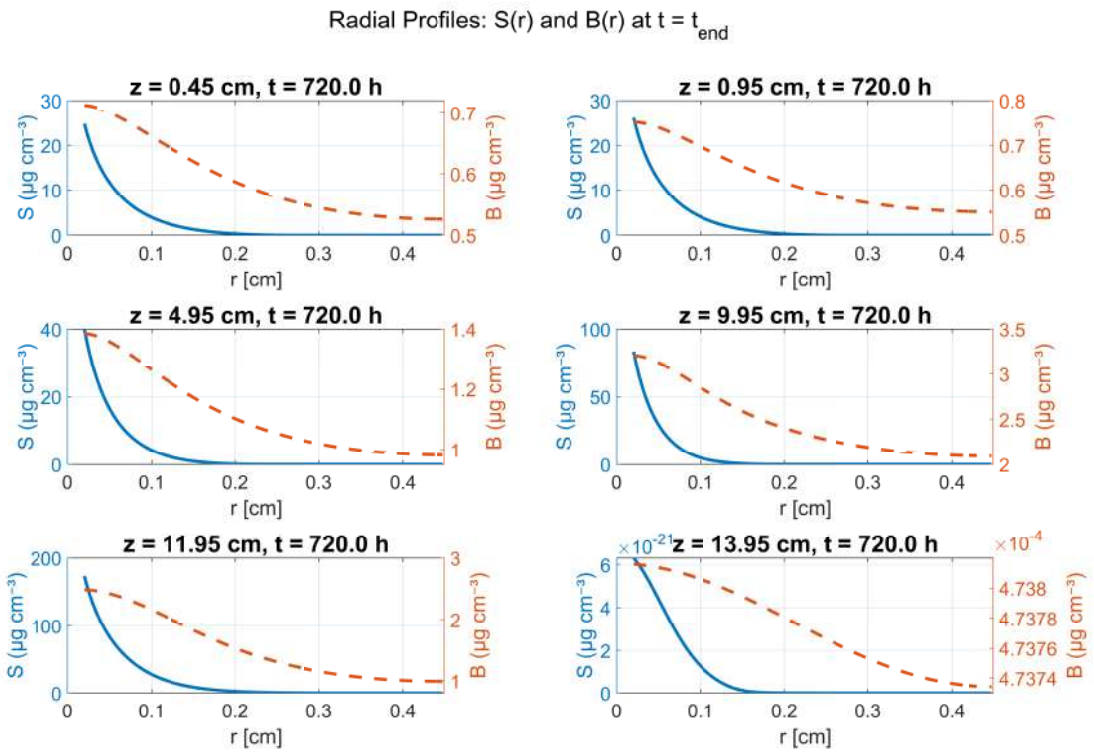

FIGURE 11. Radial concentration profiles of substrate S (left) and bacterial biomass B (right) at $t = 720$ h for several soil depths z.

maximum of only 192 µg cm^{-3} compared with the values exceeding 1000 µg cm^{-3} observed under low diffusivity. This change in the substrate profile directly affects the microbial population dynamics by improving bacterial access to the nutrient across a larger soil volume. Figure 10 (bottom) shows that the peak bacterial biomass reaches 4.0 µg cm^{-3}. Notably, at the end of the 720 h simulation, the greater spatial mobility of the substrate allows colonies to establish in zones very close to the root tip. The enhanced spatial distribution of the substrate effectively expands the habitable zone for the bacteria, reducing localized competition and allowing the population to thrive over a broader radial extent.

To examine the spatial structure of this scenario in more detail, radial concentration profiles were extracted at several soil depths z at the end of the simulation period ($t = 720$ h, Figure 11). At all depths examined, the highest microbial density is located at the root–soil interface ($r = a$) and decays sharply with increasing radial distance, reflecting the combined effect of chemotaxis and bacterial motility in organizing the biomass distribution. The substrate profiles define a zone of influence that extends radially to approximately 0.1 cm, beyond which the concentration becomes negligible. The depth-dependent variation in profile magnitude reveals the longitudinal gradient embedded in the model: younger root sections near the apex display more dynamic substrate profiles, whereas in the upper zones the bacterial population has stabilized consumption, sustaining low but steady residual substrate levels.

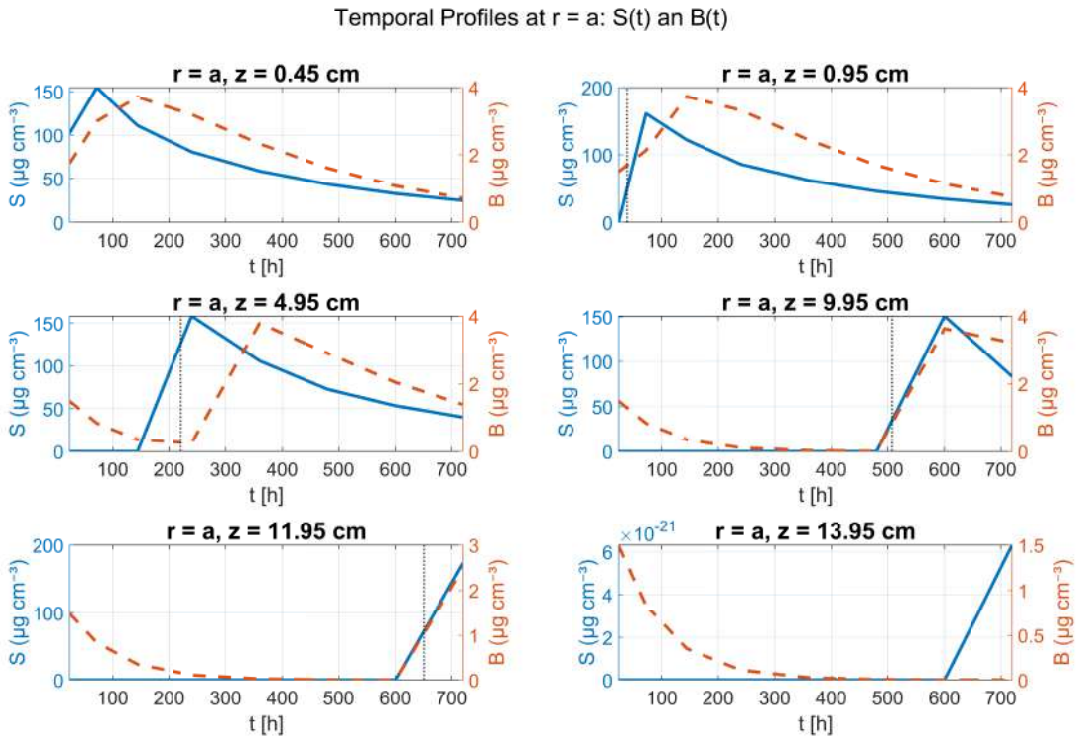

FIGURE 12. Temporal profiles of substrate S (blue) and bacterial biomass B (orange) at $r = a$ for different depths z. The dashed line marks the time at which the root tip reaches each depth $L_{\mathrm{R}}(t) = z$.

The temporal dynamics of both variables at the root–soil interface ($r = a$) are presented in Figure 12. The substrate profile (blue curve) shows an initial rapid increase driven by the constant exudation flux, followed by a pronounced decrease attributable to bacterial metabolic activity. The biomass curve exhibits an initial lag phase representing the adaptation period required for the population to initiate resource consumption and subsequent duplication. After 720 h of simulation, the bacterial biomass has not yet attained a steady state and retains a growing trend.

Near the root tip ($z \approx 14$ cm), a qualitatively distinct behavior is observed: the substrate concentration rises sharply while bacterial biomass remains virtually zero. This occurs because the root apex represents newly formed tissue that has only recently come into contact with the surrounding soil; although exudation has already commenced, the bacteria have not yet had sufficient time to colonize that region. This result demonstrates that root elongation proceeds faster than the capacity of the bacterial population to establish itself at the growing tip.

Finally, exploiting the axial-symmetry assumption, the two-dimensional solution was revolved to generate a three-dimensional visualization of the rhizosphere. The substrate plume (Figure 13(a)) appears as a system of concentric cylinders around the root, and the bacterial biomass (Figure 13(b)) forms a peripheral layer whose density peaks at a section preceding the root apex. These 3D representations clearly illustrate the spatial separation between the newest root tissue and the established bacterial colonies, highlighting the temporal lag in the colonization process.

(a) (b)

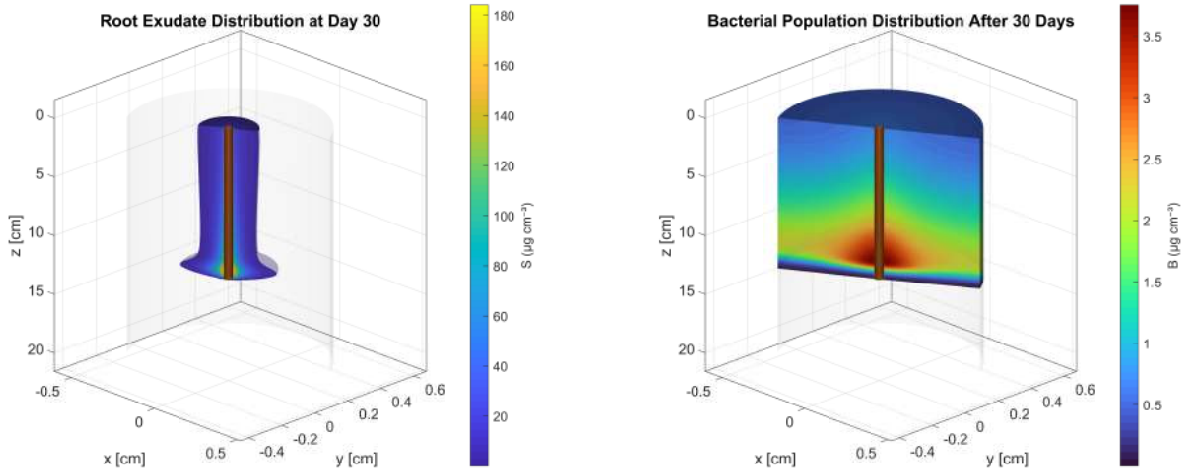

FIGURE 13. Three-dimensional visualization of the concentrations of (a) the substrate S, (b) the biomass B obtained by axial rotation of the 2D solution around the root axis.

4.2.8. *Example 9: theoretical scenario with an extended rhizosphere.* To address the question of optimizing the use of inoculated bacteria in rice seeds, a hypothetical scenario was evaluated in which the rhizosphere radius was extended to $b = 1\,\text{cm}$, considerably beyond the $0.45\,\text{cm}$ typically reported in the literature. All other parameters were kept as in Example 8, modifying only the rhizosphere extent. The model predicts bacterial dispersal reaching regions near $r = 1$ cm; however, the concentrations achieved in those zones are very low (Figure 14), suggesting that substrate availability limits effective colonization in distant zones. The highest substrate concentration recorded was $188.9\,\mu\text{g}\,\text{cm}^{-3}$, while the biomass peaked at $2.8\,\mu\text{g}\,\text{cm}^{-3}$. This confirms that the natural limitation of substrate diffusion effectively restricts the spatial boundaries of the active rhizosphere, preventing significant bacterial establishment beyond a minimal radial distance.

4.3. **Example 10: simulations with experimental growth rates.** To assess the capacity of the model to represent the spatiotemporal dynamics of real bacterial strains, two isolates from the study of [12], conducted in collaboration with the Instituto de Innovación Agropecuaria de Panamá (IDIAP), were considered. Both strains were isolated from local soil samples and shown to promote growth in rice seeds. Strain 24, identified as *Lysinibacillus fusiformis*, and Strain 59, identified as *Bacillus cereus*, were selected on the basis of their ability to proliferate in ASHBY medium, a selective nitrogen-free medium whose use confirms their capacity as nitrogen-fixing bacteria, a desirable trait for biofertilizer applications. Maximum growth rates estimated from the experimental data were $\mu_{\max} = 0.1449\,\text{h}^{-1}$ for Strain 24 and $\mu_{\max} = 0.1432\,\text{h}^{-1}$ for Strain 59. Given the near-identical values, a unified rate $\mu = 0.14\,\text{h}^{-1}$ was adopted for both strains. All other parameters were kept as in Example 8, so that this scenario differs from it only in the bacterial growth rate, reduced from $0.30\,\text{h}^{-1}$ to the experimental value $0.14\,\text{h}^{-1}$.

Figure 15 (top) shows the spatial evolution of the substrate concentration profile $S(r, z)$ over $720\,\text{h}$. The highest exudation rate accompanies the root apex as it advances into deeper soil layers

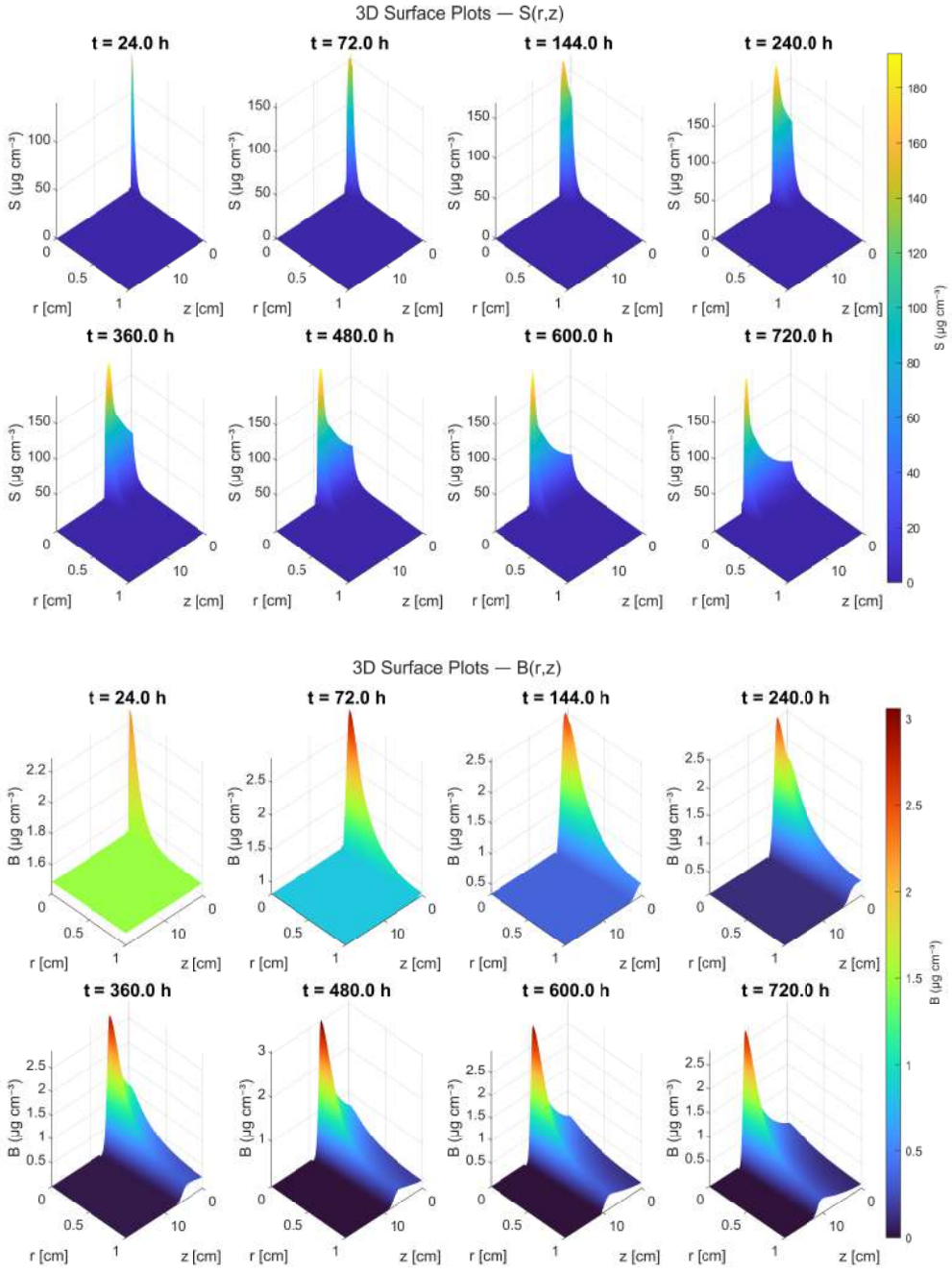

FIGURE 14. Example 9 (theoretical scenario with an extended rhizosphere): simulated concentration of (top) substrate S and (bottom) bacterial biomass B with an extended rhizosphere radius $b = 1\,\text{cm}$ at eight time instants.

(direction z), establishing the chemotactic field that drives microbial migration. The corresponding bacterial dynamics (Figure 15, bottom) reveal the capacity of the model to capture complex biological phenomena. During the first 144 h, bacteria begin concentrating in the upper soil layers in response to the initial exudates. From 360 h onward, a clear chemotactic effect emerges: the

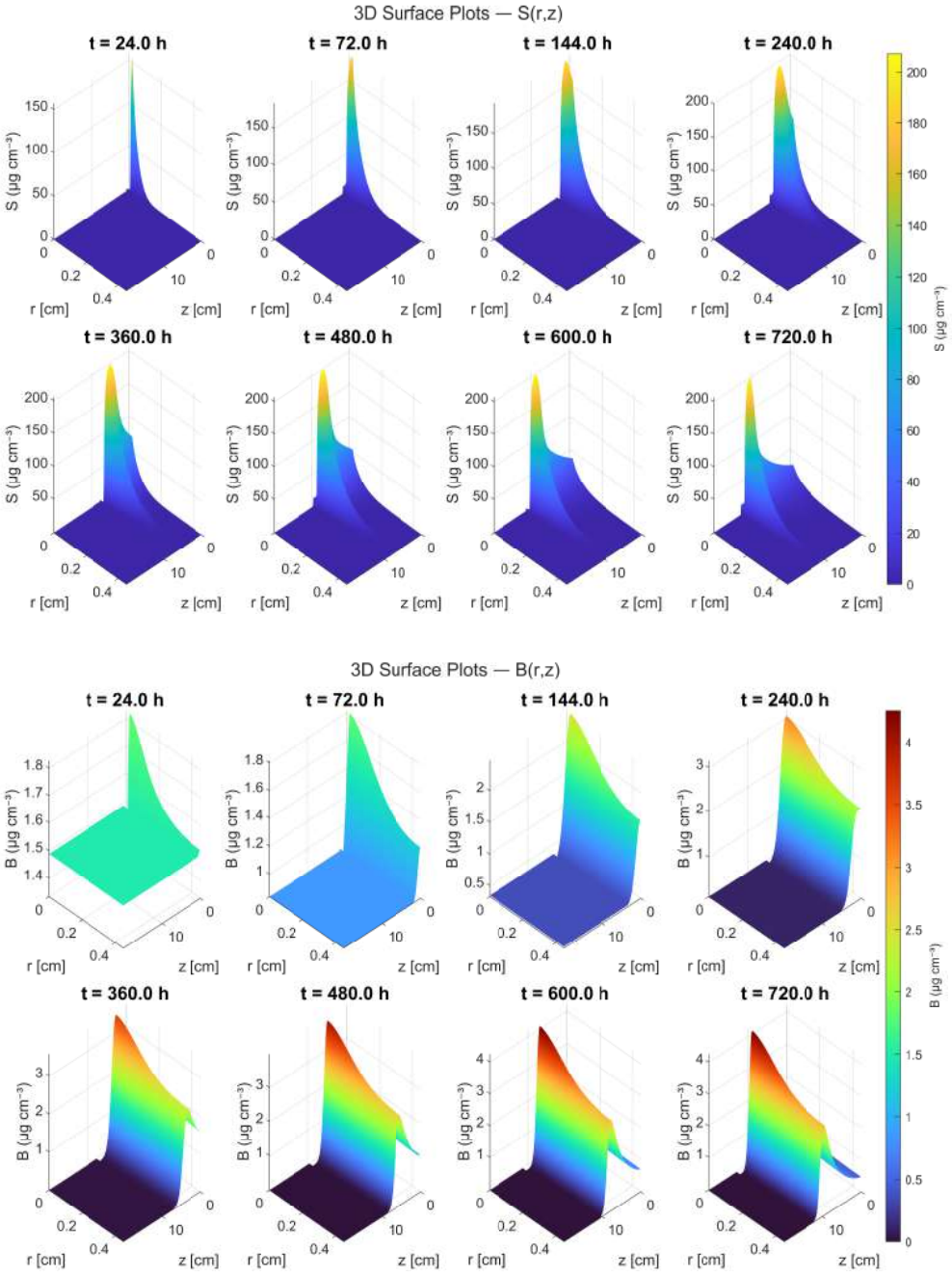

FIGURE 15. Example 10 (simulations with experimental growth rates): simulated concentration of (top) substrate S and (bottom) bacterial biomass B with the unified IDIAP growth rate ($\mu = 0.14\,\mathrm{h}^{-1}$ [12]) at eight time instants.

zone of maximum bacterial concentration migrates downward, tracking the substrate peak at the advancing root tip through directed motility and local resource consumption.

5. Conclusions and Future Work

In this work, a system of partial differential equations was formulated to describe the growth, dispersion, and colonization dynamics of plant growth-promoting bacteria (PGPR) in the rice rhizosphere. The model couples substrate diffusion with bacterial reaction, motility, and chemotaxis, the latter acting as a key mechanism governing colonization, and represents the interaction between root exudates and microbial biomass in an axisymmetric domain with a moving boundary that tracks root elongation.

A numerical algorithm was designed and implemented to approximate the solutions of the proposed system, combining a finite volume method for spatial discretization with an IMEX-θ time-integration scheme that treats the stiff diffusion terms implicitly and the reaction and chemotaxis terms explicitly. Through an M-matrix analysis of the resulting linear systems, the fully discrete scheme was shown to preserve the non-negativity of both substrate and biomass under a CFL condition, avoiding the ad hoc clipping of negative values.

Computational simulations were carried out by varying the main model parameters. The results reveal the formation of spatial concentration gradients of both substrate and bacterial biomass around the root, with the highest bacterial concentration localizing slightly ahead of the root tip after 30 days. The parameter analysis indicates that the substrate diffusion coefficient is a dominant factor in colonization: lower values favor the retention of exudates in the root environment and, consequently, their uptake by bacteria, whereas increases in bacterial motility, growth rate, and initial population all accelerate colonization of the soil. The scheme was validated against the one-dimensional, single-equation case of the reference literature, with consistent behavior observed.

A theoretical scenario with an extended rhizosphere was subsequently examined, showing that effective bacterial dispersal reaches distant regions only at very low concentrations, becoming negligible beyond a short radial distance. Furthermore, by incorporating the experimental growth rate provided by the IDIAP for two promising strains, *Lysinibacillus fusiformis* and *Bacillus cereus*, the model demonstrated that, starting from a single empirical population-growth datum obtained *in vitro*, it is possible to predict the asymmetric spatial distribution of bacteria in the rhizosphere over one month of continuous growth.

Compared with previous models, the present work considered two-dimensional dispersion, simultaneously incorporated the dynamics of both exudate and bacteria, assumed non-constant exudation, and modeled the process from the onset of root growth over a 30-day period. Nevertheless, a simplified root geometry, a straight cylinder, was assumed, which constitutes an idealization relative to the real structure, particularly in rice crops where root hairs introduce additional structural complexity.

Future work will proceed along several directions. A natural and biologically important extension is to couple the bacterial dynamics back to root development: in the present model the root elongation $L_R(t)$ is prescribed independently of the microbial population, whereas PGPR are known to stimulate root growth, so that incorporating the effect of bacterial colonization on root growth would close this feedback loop. The straight-cylinder root could also be replaced by more realistic architectures accounting for root hairs and lateral branching, particularly relevant for rice, and the homogeneous-soil assumption relaxed to include spatial heterogeneity and anisotropy of the transport coefficients. The biological model can be further enriched by including competition with the native microbial community, predation, and biofilm formation, which were neglected here.

CRediT authorship contribution statement

I. Arrocha: Conceptualization, Methodology, Software. **R. Bürger:** Formal analysis, Methodology, Supervision, Writing – original draft, Writing – review & editing. **M. Gómez:** Conceptualization, Formal analysis, Methodology, Software, Supervision, Writing – original draft, Writing – review & editing. **Y. Vásquez:** Formal analysis, Methodology, Supervision, Writing - original draft, Writing – review & editing.

Declaration of Competing Interest

The authors declare that there is no competing interest.

Acknowledgments

R.B. is supported by ANID (Chile) through Fondecyt project 1250676 and Centro de Modelamiento Matemático (CMM), BASAL project FB210005. M.G. is supported by the Instituto para la Formación y Aprovechamiento de Recursos Humanos (IFARHU) and the Secretaría Nacional de Ciencia, Tecnología e Innovación (SENACYT), Panama [grant number 270-2024-130]. Y.V. is supported by the Sistema Nacional de Investigación (SNI), SENACYT, Panama. The authors thank the Instituto de Innovación Agropecuaria de Panamá (IDIAP) for providing the experimental data used in this work.

Data availability

No additional data were used beyond those reported in the article.

References

[1] Instituto Nacional de Estadística y Censo (INEC), *Superficie sembrada y cosecha de arroz: año agrícola 2024–25*, Panama, 2025. Available from https://www.inec.gob.pa

[2] Ministerio de Desarrollo Agropecuario (MIDA), *Producir más con menos, un objetivo del MIDA para el rendimiento del arroz panameño*, 2024. https://mida.gob.pa/2024/09/17/producir-mas-con-menos-un-objetivo-del-mida-para-el-rendimiento-del-arroz-panameno/

[3] E. M. Estabrook and J. I. Yoder, Plant-plant communications: Rhizosphere signaling between parasitic angiosperms and their hosts, Plant Physiol. 116 (1998) 1–7.

[4] M. Ahemad and M. Kibret, Mechanisms and applications of plant growth promoting rhizobacteria: Current perspective, J. King Saud Univ. Sci. 26 (2014) 1–20. https://doi.org/10.1016/j.jksus.2013.05.001

[5] G. Lazarovits and J. Nowak, Rhizobacteria for improvement of plant growth and establishment, HortScience 32 (1997) 188–192. https://doi.org/10.21273/HORTSCI.32.2.188

[6] M. Z. Iqbal, K. Singh, and R. Chandra, Recent advances of plant growth promoting rhizobacteria (PGPR) for eco-restoration of polluted soil, Cleaner Eng. Technol. 19 (2024) 100845. https://doi.org/10.1016/j.clet.2024.100845

[7] F. D. Dakora and D. A. Phillips, Root exudates as mediators of mineral acquisition in low-nutrient environments, Plant Soil 245 (2002) 35–47. https://doi.org/10.1023/A:1020809400075

[8] H. E. Flores, J. M. Vivanco, and V. M. Loyola-Vargas, "Radicle" biochemistry: The biology of root-specific metabolism, Trends Plant Sci. 4 (1999) 220–226. https://doi.org/10.1016/S1360-1385(99)01411-9

[9] B. G. Kang, W. T. Kim, H. S. Yun, and S. C. Chang Use of plant growth-promoting rhizobacteria to control stress responses of plant roots, Plant Biotechnol. Rep. 4 (2010) 179–183. https://doi.org/10.1007/s11816-010-0136-1

[10] A. Sharma, D. Shankhdhar, A. Sharma, and S. C. Shankhdhar, Growth promotion of the rice genotypes by PGPRs isolated from rice rhizosphere, J. Soil Sci. Plant Nutr. 14 (2014) 505–517. https://doi.org/10.4067/S0718-95162014005000040

[11] T. A. Abd El-Mageed, S. A. Abd El-Mageed, M. T. El-Saadony, S. Abdelaziz, and N. M. Abdou, Plant growth-promoting rhizobacteria improve growth, morph-physiological responses, water productivity, and yield of rice plants under full and deficit drip irrigation, Rice 15 (2022) 38. https://doi.org/10.1186/s12284-022-00564-6

[12] O. Causadías et al., *Evaluación del efecto de bacterias promotoras del crecimiento vegetal en el cultivo de arroz en Panamá*, Master's thesis, Universidad Tecnológica de Panamá, 2023.
[13] C. W. Kuppe, A. Schnepf, E. von Lieres, M. Watt, and J. A. Postma, Rhizosphere models: their concepts and application to plant-soil ecosystems, Plant Soil 474 (2022) 17–55. https://doi.org/10.1007/s11104-021-05201-7
[14] E. M. Scott, A. K. Rattray, J. I. Prosser, K. Killham, C. D. Campbell, and L. A. Glover, A mathematical model for dispersal of bacterial inoculants colonizing the wheat rhizosphere, Soil Biol. Biochem. 27 (1995) 1307–1318. https://doi.org/10.1016/0038-0717(95)00050-O
[15] N. S. Strigul and L. V. Kravchenko, Mathematical modeling of PGPR inoculation into the rhizosphere, Environ. Model. Softw. 8 (2006) 1158–1171. https://doi.org/10.1016/j.envsoft.2005.06.003
[16] E. I. Newman and A. Watson, Microbial abundance in the rhizosphere: A computer model, Plant Soil 48 (1977) 17–56. https://doi.org/10.1007/BF00015157
[17] A. Cornish-Bowden, One hundred years of Michaelis-Menten kinetics, Perspect. Sci. 4 (2015) 3–9. https://doi.org/10.1016/j.pisc.2014.12.002
[18] H. de Parseval, S. Barot, J. Gignoux, J.-C. Lata, and X. Raynaud, Modelling facilitation or competition within a root system: importance of the overlap of root depletion and accumulation zones, Plant Soil 419 (2017) 1–15. https://doi.org/10.1007/s11104-017-3321-y
[19] A. M. Turing, The chemical basis of morphogenesis, Philos. Trans. R. Soc. Lond. B 237 (1952) 37–72. https://doi.org/10.1098/rstb.1952.0012
[20] K. Kawasaki, A. Mochizuki, M. Matsushita, T. Umeda, and N. Shigesada, Modeling spatio-temporal patterns generated by *Bacillus subtilis*, J. Theoret. Biol. 188 (1997) 177–185. https://doi.org/10.1006/jtbi.1997.0462
[21] M. Mimura, H. Sakaguchi, and M. Matsushita, Reaction-diffusion modelling of bacterial colony patterns, Phys. A 282 (2000) 283–303. https://doi.org/10.1016/S0378-4371(00)00085-6
[22] A. M. Lacasta, I. R. Cantalapiedra, C. E. Auguet, A. Peñaranda, and L. Ramírez-Piscina, Modeling of spatiotemporal patterns in bacterial colonies, Phys. Rev. E 59 (1999) 7036–7041. https://doi.org/10.1103/PhysRevE.59.7036
[23] J. D. Murray, Mathematical Biology II: Spatial Models and Biomedical Applications, 3rd ed., Springer, New York, 2003.
[24] E. F. Keller and L. A. Segel, Model for chemotaxis, J. Theoret. Biol. 30 (1971) 225–234. https://doi.org/10.1016/0022-5193(71)90050-6
[25] G. Arumugam and J. Tyagi, Keller-Segel chemotaxis models: A review, Acta Appl. Math. 171 (2021) 6. https://doi.org/10.1007/s10440-020-00374-2
[26] T. Hillen and K. J. Painter, A user's guide to PDE models for chemotaxis, J. Math. Biol. 58 (2009) 183–217. https://doi.org/10.1007/s00285-008-0201-3
[27] J. F. Leyva, C. Málaga, and R. G. Plaza, The effects of nutrient chemotaxis on bacterial aggregation patterns with non-linear degenerate cross diffusion, Phys. A 392 (2013) 5644–5662. https://doi.org/10.1016/j.physa.2013.07.022
[28] E. Lankeit and J. Lankeit, On the global generalized solvability of a chemotaxis model with signal absorption and logistic growth terms, Nonlinearity **32** (2019) 1569–1596. https://doi.org/10.1088/1361-6544/aaf8c0
[29] L. Dupuy and W. K. Silk, Mechanisms of early microbial establishment on growing root surfaces, Vadose Zone J. 15 (2016) 1–13. https://doi.org/10.2136/vzj2015.06.0094
[30] R. J. LeVeque, Finite Volume Methods for Hyperbolic Problems, Cambridge University Press, Cambridge, 2002.
[31] F. Moukalled, L. Mangani, and M. Darwish, The Finite Volume Method in Computational Fluid Dynamics, Springer, Cham, Switzerland, 2016. https://doi.org/10.1007/978-3-319-16874-6
[32] R. Eymard, T. Gallouët, and R. Herbin, The Finite Volume Method, in: Handbook of Numerical Analysis, Vol. VII, North-Holland, Amsterdam, 2000, pp. 713–1018.
[33] R. J. LeVeque, Numerical Methods for Conservation Laws, Birkhäuser, Basel, 1992.
[34] E. F. Toro, Riemann Solvers and Numerical Methods for Fluid Dynamics, 3rd ed., Springer, Berlin, 2009. https://doi.org/10.1007/b79761
[35] U. M. Ascher, S. J. Ruuth, and B. T. R. Wetton, Implicit-explicit methods for time-dependent partial differential equations, SIAM J. Numer. Anal. 32 (1995) 797–823. https://doi.org/10.1137/0732037
[36] W. Hundsdorfer and J. G. Verwer, Numerical Solution of Time-Dependent Advection-Diffusion-Reaction Equations, Springer, Berlin, 2003. https://doi.org/10.1007/978-3-662-09017-6
[37] R. Bürger, S. Diehl, M. C. Martí, and Y. Vásquez, A degenerating convection–diffusion system modelling froth flotation with drainage, IMA J. Appl. Math. 87 (2022) 1151–1190. https://doi.org/10.1093/imamat/hxac033

[38] R. Bürger, J. Careaga, S. Diehl, and R. Pineda, Numerical schemes for a moving-boundary convection-diffusion-reaction model of sequencing batch reactors, ESAIM: Math. Model. Number. Anal. 57 (2023) 2931–2976. https://doi.org/10.1051/m2an/2023068

[39] C. D. Acosta, R. Bürger, J. Careaga, S. Diehl, R. Pineda, and D. Támara, A semi-implicit method for a degenerating convection-diffusion-reaction problem modeling secondary settling tanks. In: T. Morales de Luna, S. Boscarino, P. Frolkovič, L. O. Müller, and C. Escalante (eds.), Advances in Nonlinear Hyperbolic Partial Differential Equations: Numerical Analysis and Applications, ICIAM2023 Springer Series vol. 7, Springer Nature Singapore Pte Ltd., Singapore, 23–58 (2026). https://doi.org/10.1007/978-981-96-9087-9_2

[40] R. Bürger, J. Careaga, S. Diehl, and R. Pineda, A moving-boundary model of reactive settling in wastewater treatment. Part 2: Numerical scheme, Appl. Math. Model. 111 (2022) 247–269. https://doi.org/10.1016/j.apm.2022.06.030

[41] H. Schwalm, C. Staudinger, M.-R. Hajirezaei, E. Mundschenk, A. Golestanifard, M. Holz, M. Wissuwa, and E. Oburger, Root exudation patterns of contrasting rice (*Oryza sativa* L.) lines in response to P limitation, Planta 260 (2024) 123. https://doi.org/10.1007/s00425-024-04556-2

[42] R. Bürger, S. Diehl, M. C. Martí, and Y. Vásquez, A numerical scheme for a model of a flotation column including the transport of liquid components, ESAIM: Math. Model. Numer. Anal., to appear. https://doi.org/10.1051/m2an/2026050

[43] L. A. Segel, I. Chet, and Y. Henis, A simple quantitative assay for bacterial motility, J. Gen. Microbiol. 98 (1977) 329–337. https://doi.org/10.1099/00221287-98-2-329

[44] P. H. Nye, Changes of pH across the rhizosphere induced by roots, Plant Soil 61 (1981) 7–26. https://doi.org/10.1007/BF02277359

[45] L. V. Kravchenko, N. S. Strigul', and I. A. Shvytov, Mathematical simulation of the dynamics of interacting populations of rhizosphere microorganisms, Microbiology 73 (2004) 189–195. https://doi.org/10.1023/B:MICI.0000023988.11064.43

[46] L. F. Gómez, *Desarrollo y aplicación de una estrategia de biofertilización en plantas de arroz (oryza sativa l.) empleando microorganismos promotores de crecimiento vegetal*, Master's thesis, Universidad Nacional de Colombia, Medellín, 2015. https://repositorio.unal.edu.co/items/c20aa5c7-3266-41b7-a183-5e219b83767c

[47] H. Schwalm, C. Staudinger, M.-R. Hajirezaei, E. Mundschenk, A. Golestanifard, M. Holz, M. Wissuwa, and E. Oburger, Root exudation patterns of contrasting rice (*Oryza sativa* L.) lines in response to P limitation: supplementary information, https://link.springer.com/article/10.1007/s00425-024-04556-2

[48] C. W. Kuppe, G. J. D. Kirk, M. Wissuwa, and J. A. Postma, Rice increases phosphorus uptake in strongly sorbing soils by intra-root facilitation, Plant Cell Environ. 45 (2022) 884–899. https://doi.org/10.1111/pce.14285

[49] J. Nestler, S. D. Keyes, and M. Wissuwa, Root hair formation in rice (*Oryza sativa* L.) differs between root types and is altered in artificial growth conditions, J. Exp. Bot. 67 (2016) 3699–3708. https://doi.org/10.1093/jxb/erw115

[50] X. Wei, T. Ge, Z. Zhu, Y. Hu, S. Liu, Y. Li, J. Wu, and B. S. Razavi, Expansion of rice enzymatic rhizosphere: temporal dynamics in response to phosphorus and cellulose application, Plant Soil 445 (2019) 169–181. https://doi.org/10.1007/s11104-018-03902-0

[51] T. Ge, X. Wei, B. S. Razavi, Z. Zhu, Y. Hu, Y. Kuzyakov, D. L. Jones, and J. Wu, Stability and dynamics of enzyme activity patterns in the rice rhizosphere: effects of plant growth and temperature, Soil Biol. Biochem. 113 (2017) 108–115. https://doi.org/10.1016/j.soilbio.2017.06.005

Centro de Investigación en Ingeniería Matemática (CI^{2}MA)

PRE-PUBLICACIONES 2026

2026-10 Aníbal Coronel, Fernando Huancas, Mauricio Sepúlveda: *Identification of a power-like reaction term in a reaction-diffusion SIS model*

2026-11 Esteban Henriquez, Manuel Solano: *An unfitted HDG method for a distributed optimal convection-diffusion control problem*

2026-12 Sergio Caucao, Gabriel N. Gatica, Luis F. Gatica, Cristian Inzunza: *A priori and a posteriori error analysis of a mixed FEM for stationary convective Brinkman-Forchheimer flows with variable porosity*

2026-13 Jessika Camaño, Ricardo Oyarzúa, Katherine Rojo, Segundo Villa-Fuentes: *A mixed finite element method based on pseudostress and stream-function for the Navier–Stokes problem in 2D*

2026-14 Raimund Bürger, Cipriano Escalante, Enrique D. Fernández Nieto, Jorge Moya: *A two-dimensional multilayer shallow water model of tsunami-forest interaction*

2026-15 Alonso J. Bustos, Sergio Caucao: *A posteriori error analysis of two mixed formulations for a coupled Brinkman–Forchheimer and convection-diffusion-reaction system*

2026-16 Gabriel N. Gatica, Salim Meddahi, Kevin W. Pucha-Atan, Ricardo Ruiz-Baier: *A Banach spaces-based fully mixed finite element method for the thermo-electro-hydrodynamic Boussinesq problem*

2026-17 Tomás Barrios, Edwin Behrens, Rommel Bustinza, Jose M. Cascon: *A stabilized displacement - stress formulation for a linear elasticity problema with mixed boundary conditions*

2026-18 Gonzalo A. Benavides, Sergio Caucao, Gabriel N. Gatica, Yuri D. Sobral: *New Banach spaces-based mixed finite element methods for steady-state flows of magnetic fluids*

2026-19 Fahim Aslam, Marcelo Cavalcanti, Zayd Hajjej, You Haiyang Lin Bo, Mauricio Sepúlveda: *Blow-up of a Lamé system with fractional damping and infinite memory: theoretical and numerical study*

2026-20 Gabriel N. Gatica, Salim Meddahi: *A hybridizable discontinuous Galerkin method for the elasto–acoustic transmission problem*

2026-21 Idulfo Arrocha, Raimund Bürger, María Gómez, Yolanda Vásquez: *Modeling and numerical simulation of the colonization of plant growth-promoting bacteria in the rice rhizosphere*

Para obtener copias de las Pre-Publicaciones, escribir o llamar a: Director, Centro de Investigación en Ingeniería Matemática, Universidad de Concepción, Casilla 160-C, Concepción, Chile, Tel.: 41-2661324, o bien, visitar la página web del centro: `http://www.ci2ma.udec.cl`




Centro de Investigación en
Ingeniería Matemática (CI²MA)
Universidad de Concepción

Casilla 160-C, Concepción, Chile
Tel.: 56-41-2661324/2661554/2661316
http://www.ci2ma.udec.cl